Ch. F. Markides · S. K. Kourkoulis

The finite circular disc with a central elliptic hole under parabolic pressure

Abstract The mechanical response of a finite circular disc with a central elliptic hole is modelled mathematically assuming that the disc is subjected to radial pressure varying according to a parabolic law along two finite arcs of its periphery. The symmetry axis of the pressure forms an arbitrary angle with respect to the major axis of the elliptic hole. Using the complex potentials technique, the displacement and stress fields are determined in the form of infinite series. Assuming then that the short semi-axis of the elliptic hole tends to zero, compact expressions are obtained for the stress intensity factors characterizing the severity of the stress field around the end points of the ellipse's major axis, which now becomes the tips of a discontinuity resembling a mathematic crack. The solution for the stress intensity factors is validated against the respective one proposed by Atkinson et al. in the limiting case of a centrally cracked disc under diametral compressive point forces. The agreement is very good as long as the length of the crack does not exceed the disc's radius. The novelty of the present solution (besides imposing parabolic pressure instead of uniform one or point forces) is that the discontinuity covers the whole range from the circular hole (ring) to the mathematical crack. Moreover, the expressions obtained are exact, complete and easily programmable. From a practical point of view, the solution introduced can be proven a valuable, easy-to-use tool for engineers using the Brazilian-disc test for the determination of fracture toughness of brittle geomaterials. Indeed, the parabolic pressure considered here approaches closely the actual load distribution exerted on the disc during the standardized implementation of the test. In addition, the form of discontinuity considered here is closer to the shape of the cracks actually machined in the specimens of the test which are by no means mathematical cuts but rather they are slits with a finite distance between their lips.

1 Introduction

Modelling the mechanical response (or in other words determining the stress and displacement fields) of a body of finite dimensions subjected to an external mechanical load is usually a challenging task. The presence of geometric discontinuities (usually in the form of cracks and holes) makes things even more difficult. As a result, analytic closed-form solutions do not exist even in the case of relatively simple configurations.

Among these configurations, of increased practical interest is the circular disc with a central non-mathematic crack (i.e. a crack which is not simulated by an ideal cut of zero distance between its lips) the length of which is not very small with respect to the disc's diameter. The specific configuration is the basis of the technique widely used to determine the fracture toughness, K_{IC}, of brittle materials either in the form of Cracked Chevron Notched Brazilian Disc (CCNBD) or in the form of the Cracked Straight Through Brazilian Disc (CSTBD).

Ch. F. Markides · S. K. Kourkoulis (✉)
Department of Mechanics, School of Applied Mathematical and Physical Sciences, National Technical University of Athens,
5 Heroes of Polytechnion Avenue, Theocaris Bld., Zografou Campus, 157 73 Athens, Greece
E-mail: stakkour@central.ntua.gr
Tel.: +30 210 7721263

The respective procedure has is long ago been standardized by the International Society for Rock Mechanics [1]. The importance of the specific standard is clearly understood by taking into account that fracture toughness quantifies the resistance of a cracked body to further extension of the pre-existing crack (crack initiation and crack propagation), and therefore, its knowledge is sine qua non for quite a few engineering applications as it is for example rock drilling and cutting, rock slope study, hydraulic fracturing, underground excavations, tunnelling, etc.

In spite of this increased practical importance, there are, even today, some open questions about the applicability of the specific standard [2,3] and the accuracy of its final outcome. To the authors' opinion, among the most controversial aspects of the standard is the one related to the exact formulae of the respective stress intensity factors (SIFs): the main obstacle hard to overcome is that the crack usually machined in a disc made of a brittle geomaterial is neither a mathematic cut nor a rectangular hole. Moreover, for practical reasons, the length of the machined crack cannot be very short (it is mentioned, for example, that according to Dong [4] "… the recommended range of the relative crack length is between 0.4 and 0.6" (with respect to the disc's diameter)).

It is emphasized from the very beginning that the specific problem (i.e. to determine the SIFs in a cracked circular disc of finite radius) is extremely complicated and it is not expected that closed solutions can be reached, unless simplifying assumptions are introduced. Such an attempt was recently proposed considering a finite centrally cracked disc under the assumption that the crack is a mathematic cut of very small length (compared to the disc's radius) and that the disc is loaded by uniformly distributed radial pressure along two finite arcs of its periphery [5]. Although that solution is closer to reality compared to previous ones (which have considered, for example, a centrally cracked disc under anti-diametral point forces [6]), there are still some points restricting its applicability in engineering practice. The most critical ones are the consideration of a mathematic cut instead of a crack with finite distance between its lips and the simulation of the load applied as uniformly distributed pressure.

In this context, an attempt is here described to relax the above two restricting assumptions. To achieve this goal, a finite circular disc with a central elliptic hole is considered subjected to a radial pressure distribution which varies along the disc's loaded arcs according to a parabolic law. The specific problem is here solved by determining first the complex potentials that characterize the equilibrium of the elliptically perforated disc adopting the method introduced by Kolosov [7] and Muskhelishvili [8]. Given the complex potentials, one can determine the stress and displacement fields all over the disc's area. Moreover, one can then determine the SIFs assuming that the minor semi-axis of the elliptic hole becomes very small compared to the long one or equivalently that the elliptic hole tends to become a crack. The solutions for both the stress and displacement fields and also for the SIFs are obtained in series form, and the respective expressions (although rather lengthy) are compact and easily programmable.

The formulae for the SIFs are validated against older, widely accepted solutions, and especially against the formulae of the pioneering work by Atkinson et al. [6], assuming that the loaded arc (which is of finite length in the present study) becomes very small so that the loading scheme becomes that of a line force (uniformly distributed along a single generatrix of the disc's lateral surface). The comparison is very satisfactory as long as the length of the crack does not exceed the disc's radius, which is a critical threshold in case the results are to be used for the determination of fracture toughness [4].

Taking advantage of the as-above-validated expressions, a parametric analysis is implemented in order for the dependence of the SIFs on some critical geometric parameters of the configuration (inclination of the crack with respect to the loading axis, disc's thickness and relative length of the crack) to be quantified. In addition, the role of the disc's material is studied, since it influences (although indirectly) the final outcome through the dependence of the loaded arc's length on the relative stiffness of the disc's–loading platen's materials.

Finally, some crucial aspects of the centrally perforated (cracked) disc, related to the contact (partial or complete) of the lips of the elliptic hole (crack) for specific orientations of the ellipse's long axis with respect to the axis of symmetry of the loading imposed, are quantitatively explored. This mutual contact of the initially stress-free crack lips was thoroughly studied already from the early seventies, in an attempt to quantify the SIFs in case of partially closed Griffith cracks [9–11]. The onset of lips contact is critical since it designates termination of the validity of the solution obtained given that the initially considered boundary conditions are strongly violated. As a last step, the limitations imposed by the fact that the friction stresses along the loaded arc were ignored during the analysis are critically discussed.
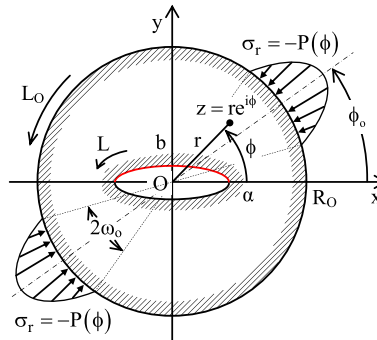
Fig. 1 Formulation of the mathematical problem and definition of symbols

2 Theoretical analysis

2.1 Formulation of the mathematical problem

Consider a circular disc of radius R_O and thickness t with a central elliptic hole L. The length of the long semi-axis of the elliptic hole is denoted by α while that of the short one is denoted by b. Assume that the disc is subjected to a parabolic pressure σ_r along two symmetric arcs of its periphery L_O, each one of length $2\omega_o$ (Fig. 1). The axis of symmetry of the pressure distribution subtends an angle ϕ_o with respect to the long axis of the elliptic hole. The elliptic hole is assumed to be completely stress free.

The problem is considered as a plane one and the disc's cross section lies at the $z = x + iy = re^{i\phi}$ complex plane. The disc's centre is considered as the origin of the Cartesian reference system xOy. Without loss of generality, it is assumed that the long axis of the elliptic hole is directed along the x-axis (Fig. 1). The radial pressure acting along $2\omega_o$ is described as:

$$\sigma_r = -P(\phi) = -P_c \left[1 - \sin^2(\phi_o - \phi)/\sin^2 \omega_o \right],$$

where $P_c = P(\phi)_{\max}$. The above pressure distribution is directly associated with the respective contact problem of a circular intact disc compressed between circular jaws of radius $R_{\mathrm{jaw}} = 1.5R_O$ [12–14], according to the respective ISRM standards [1,15]. Both P_c and ω_o are provided as functions of specific geometric and elastic characteristics of the two bodies in contact [13]. However, as it will be shown in Sect. 2.2, the pressure distribution, σ_r, may be equally well adapted also to the case of a loaded arc of arbitrarily predefined extent, equal to $2\omega_o$, by suitably adjusting the parameter P_c.

The disc is considered to be made of a homogeneous, isotropic and linearly elastic material, and Kolosov's [7] and Muskhelishvili's [8] complex potentials technique is employed for the solution of the problem.

The final target of the present study is to determine the SIFs characterizing the severity of the stress field in case the short semi-axis of the elliptic hole tends to zero or in other words in case the elliptic hole approaches a mathematic cut (crack) of length 2α.

2.2 Determination of the complex potentials

For the determination of the complex potentials characterizing the equilibrium of the circular disc with the elliptic hole, advantage is taken of a recently obtained solution for the respective problem of a circular ring [16]. According to that study, a ring of outer and inner radii R_O and R_I, respectively, and thickness t was considered subject to the same loading conditions as the ones previously described for the elliptically perforated disc (parabolic pressure distribution along two symmetric finite arcs of its periphery) when the loading symmetry axis coincided with y-axis of the Cartesian reference. For the needs of the present study, the complex potentials for the ring's elastic equilibrium obtained by Kourkoulis et al. [16] are here redefined in the Cartesian reference system shown in Fig. 1, i.e. for the case the loading symmetry axis forms the arbitrary angle ϕ_o with the x-axis, as:

$$\varphi_o(z) = \frac{P_c}{\pi} \left\{ b_0 z + \frac{B_2}{3} z^3 - B_{-2} z^{-1} \right.$$
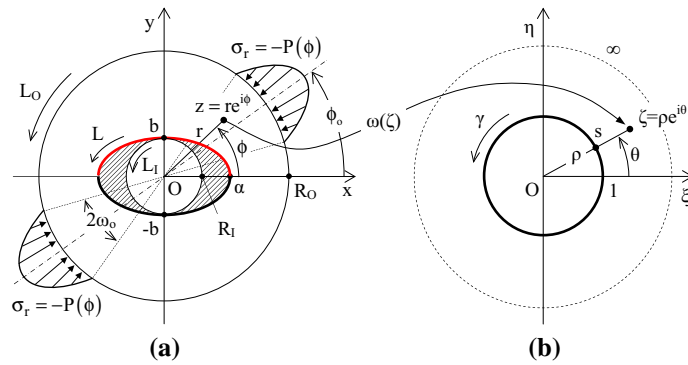
Fig. 2 The transition from the circular ring under parabolic pressure to the elliptically perforated disc (**a**) and the respective conformal mapping (**b**)

$$+ \sum_{n=1}^{\infty} \left[\frac{B_{4n}}{4n+1} z^{4n+1} - \frac{B_{-4n}}{4n-1} z^{-(4n-1)} + \frac{B_{2(2n+1)}}{4n+3} z^{4n+3} - \frac{B_{-2(2n+1)}}{4n+1} z^{-(4n+1)} \right] \right\}, \quad (1)$$

$$\psi_o(z) = \frac{P_c}{\pi} \left\{ B_0' z + \frac{B_2'}{3} z^3 - b_{-2}' z^{-1} - \frac{B_{-4}'}{3} z^{-3} \right.$$

$$\left. + \sum_{n=1}^{\infty} \left[\frac{B_{4n}'}{4n+1} z^{4n+1} + \frac{B_{2(2n+1)}'}{4n+3} z^{4n+3} - \frac{B_{-4(n+1)}'}{4n+3} z^{-(4n+3)} - \frac{B_{-2(2n+1)}'}{4n+1} z^{-(4n+1)} \right] \right\}, \quad (2)$$

where B_j, B_j' are the new values of the respective constants b_j, b_j' of Ref. [16] in the present Cartesian reference system. Especially, b_0 and b_{-2}' remain unchanged. Given their length, the respective expressions are given for brevity in "Appendix I". It is to be understood that the functions $\varphi_o(z)$ and $\psi_o(z)$ of Eqs. (1) and (2) dictate the stress and displacement states everywhere in the ring through the well-known Muskhelishvili's [8] formulae.

In order now to pass from the ring to the elliptically perforated disc, an elliptic contour L is considered, with semi-axes α and b, circumscribing the inner hole of the ring L_I so that $R_I = b$ (Fig. 2a). Removing from the ring the shadowed area between contours L and L_I, an elliptically perforated disc is obtained. Then, the complex potentials that define the elastic equilibrium of such a region will be of the form:

$$\varphi(z) = \varphi_o(z) + \varphi_*(z),$$
$$\psi(z) = \psi_o(z) + \psi_*(z), \quad (3)$$

where $\varphi_o(z)$ and $\psi_o(z)$ are given by Eqs. (1) and (2), whereas $\varphi_*(z)$ and $\psi_*(z)$ are unknown functions corresponding to the influence (disturbance in $\varphi_o(z)$ and $\psi_o(z)$) of the elliptic hole. In case L is sufficiently small, $\varphi_o(z)$ and $\psi_o(z)$ will prevail near the disc's periphery L_O. Then, it could be assumed that L_O lies at infinity, regarding L, and that $\varphi_o(z)$ and $\psi_o(z)$ govern the elastic equilibrium at remote parts of the region, which might be conceived as an infinite one. In that case, $\varphi_*(z)$ and $\psi_*(z)$ should be zero at L_O, which lies at infinity, and therefore, they must be holomorphic in the region between L and L_O, i.e. in the elliptically perforated disc.

To insert the elliptic hole L into the problem, the conformal transformation

$$z = \omega(\zeta) = R\left(\zeta + m/\zeta\right) \quad (4)$$

(with $R = (\alpha + b)/2$ and $m = (\alpha - b)/(\alpha + b)$) is introduced, mapping the part of the ring remaining on the right of L (described in the counterclockwise direction) to the mathematical $\zeta = \xi + i\eta = \rho e^{i\theta}$ complex plane with the unit hole γ (L corresponds to γ on which the point ζ is denoted by $s = e^{i\theta}$ (Fig. 2b)).

By combining Eqs. (3) and (4), and using the notation $\varphi(\zeta) = \varphi(\omega(\zeta))$ and $\psi(\zeta) = \psi(\omega(\zeta))$, one obtains the relations

$$\varphi(\zeta) = \varphi_o(\zeta) + \varphi_*(\zeta),$$
$$\psi(\zeta) = \psi_o(\zeta) + \psi_*(\zeta). \quad (5)$$

By demanding L to be free from stresses (see Eq. (6) below), the shadowed area between contours L and L_I (Fig. 2a) is essentially removed, "transforming" the ring into the elliptically perforated disc in question. In that case, the Muskhelishvili's formula [8] for the boundary conditions regarding stresses on L, becomes

$$\varphi(s) + \frac{s^2 + m}{s(1 - ms^2)}\overline{\varphi'(s)} + \overline{\psi(s)} = 0 \tag{6}$$

for s on γ; a prime denotes the first-order derivative, while an over-bar denotes the complex conjugate value. Substituting Eq. (5) into Eq. (6), it is obtained that

$$\varphi_*(s) + \frac{s^2 + m}{s(1 - ms^2)}\overline{\varphi'_*(s)} + \overline{\psi_*(s)} = -\underbrace{\left[\varphi_o(s) + \frac{s^2 + m}{s(1 - ms^2)}\overline{\varphi'_o(s)} + \overline{\psi_o(s)}\right]}_{f_*(s)}, \tag{7}$$

where, as stated before, $\varphi_*(z)$ and $\psi_*(z)$ should be conceived as functions holomorphic, vanishing at infinity. Then, according to Muskhelishvili's general formulae for infinite regions [8], the solution of Eq. (7) is written as

$$\varphi_*(\zeta) = -\frac{1}{2\pi i}\int_\gamma \frac{f_*(s)\mathrm{d}s}{s - \zeta},$$

$$\psi_*(\zeta) = -\frac{1}{2\pi i}\int_\gamma \frac{\overline{f_*(s)}\mathrm{d}s}{s - \zeta} - \zeta\frac{1 + m\zeta^2}{\zeta^2 - m}\varphi'_*(\zeta). \tag{8}$$

By combining Eqs. (1), (2), (4), (5), (7) and (8), and using properties of Cauchy's type integrals, firstly $\varphi_*(\zeta)$ and $\psi_*(\zeta)$, and in turn $\varphi(\zeta)$ and $\psi(\zeta)$ are obtained as follows:

$$\varphi(\zeta) = \frac{P_c R}{\pi}\left\{\left(b_0 + mR^2 B_2\right)\zeta + \frac{R^2 B_2}{3}\zeta^3 - \frac{mb_0 + \overline{B'_0} + R^2\left[\left(1 + 2m^2\right)\overline{B_2} + m\overline{B'_2}\right]}{\zeta}\right.$$

$$-\left(m\overline{B_2} + \frac{\overline{B'_2}}{3}\right)\frac{R^2}{\zeta^3} + \sum_{n=1}^{\infty}R^{4n}\left[\frac{B_{4n}}{4n + 1}G^\infty_{4n+1}(\zeta) - \overline{B_{4n}}G^0_{4n}(\zeta) - \frac{\overline{B'_{4n}}}{4n + 1}G^0_{4n+1}(\zeta)\right.$$

$$\left.\left.+R^2\left(\frac{B_{2(2n+1)}}{4n + 3}G^\infty_{4n+3}(\zeta) - \overline{B_{2(2n+1)}}G^0_{2(2n+1)}(\zeta) - \frac{\overline{B'_{2(2n+1)}}}{4n + 3}G^0_{4n+3}(\zeta)\right)\right]\right\}, \tag{9}$$

$$\psi(\zeta) = \frac{P_c R}{\pi}\frac{\zeta^2}{\zeta^2 - m}\left\{\left(B'_0 + \frac{2mR^2 B'_2}{3}\right)\zeta + \frac{R^2 B'_2}{3}\zeta^3 - \left(\frac{8m\overline{B_2}}{3} + \overline{B'_2}\right)\frac{R^2}{\zeta^5}\right.$$

$$-\frac{R^2\left(4\frac{1 + 3m^2}{3}\overline{B_2} + 2m\overline{B'_2}\right) + \overline{B'_0}}{\zeta^3} - 2\frac{\left(1 + m^2\right)\left(b_0 + 2mR^2\Re B_2\right) + m\Re\left(B'_0 + mR^2 B'_2\right)}{\zeta}$$

$$+\left(\frac{1}{\zeta} + m\zeta\right)\sum_{n=1}^{\infty}R^{4n}\left[\overline{B_{4n}}\frac{\mathrm{d}G^0_{4n}(\zeta)}{\mathrm{d}\zeta} - \frac{B_{4n}}{4n + 1}\frac{\mathrm{d}G^\infty_{4n+1}(\zeta)}{\mathrm{d}\zeta} + \frac{\overline{B'_{4n}}}{4n + 1}\frac{\mathrm{d}G^0_{4n+1}(\zeta)}{\mathrm{d}\zeta}\right.$$

$$\left.+R^2\left(\overline{B_{2(2n+1)}}\frac{\mathrm{d}G^0_{2(2n+1)}(\zeta)}{\mathrm{d}\zeta} - \frac{B_{2(2n+1)}}{4n + 3}\frac{\mathrm{d}G^\infty_{4n+3}(\zeta)}{\mathrm{d}\zeta} + \frac{\overline{B'_{2(2n+1)}}}{4n + 3}\frac{\mathrm{d}G^0_{4n+3}(\zeta)}{\mathrm{d}\zeta}\right)\right]$$

$$-\left(1 - \frac{m}{\zeta^2}\right)\sum_{n=1}^{\infty}R^{4n}\left[\frac{\overline{B_{4n}}}{4n + 1}G^0_{4n+1}(\zeta) - B_{4n}G^\infty_{4n}(\zeta) - \frac{B'_{4n}}{4n + 1}G^\infty_{4n+1}(\zeta)\right.$$

$$\left.\left.+R^2\left(\frac{\overline{B_{2(2n+1)}}}{4n + 3}G^0_{4n+3}(\zeta) - B_{2(2n+1)}G^\infty_{2(2n+1)}(\zeta) - \frac{B'_{2(2n+1)}}{4n + 3}G^\infty_{4n+3}(\zeta)\right)\right]\right\}. \tag{10}$$

In Eqs. (9) and (10), the symbol $\Re$ denotes the real part. Moreover $G_j^\infty(\zeta)$ and $G_j^0(\zeta)$ are the principal parts of analytic functions involved during the solution at the point at infinity and at $\zeta = 0$, respectively. Again for brevity, their analytic expressions are given (in the order they appear in Eqs. (9) and (10)) in "Appendix II".

At this point, it must be mentioned that the value of P_c as well as that of the extent of the loaded semi-arc ω_o, entering into the above formulae through the constants b_0, B_j and B_j', can be either provided by the solution of a contact problem or arbitrarily prescribed at one's convenience. For example, assuming that upon being squeezed between the jaws of the ISRM-suggested device for the implementation of the Brazilian-disc test under an overall load P_{frame}, the elliptically perforated disc behaves, in the immediate vicinity of the contact arc, like the intact one, it can be written that [13]:

$$\omega_o = \arcsin\sqrt{\frac{6K P_{\text{frame}}}{\pi R_O t}}, \quad P_c = P(\phi)_{\max} = \sqrt{\frac{3\pi P_{\text{frame}}}{32 K R_O t}}, \quad K = \frac{\kappa + 1}{4\mu} + \frac{\kappa_J + 1}{4\mu_J}, \tag{11}$$

where κ, κ_J and μ, μ_J are Muskhelishvili's constants and the shear moduli of the materials of the elliptically perforated disc and the jaw, respectively.

On the contrary, for the second choice (i.e. in case arbitrary values are to be ascribed to ω_o), it is readily seen that for static equivalence to be maintained, the following relation between ω_o and P_c must hold:

$$P_c = P(\phi)_{\max} = \frac{P_{\text{frame}}}{2R_O \omega_o t} \cdot \frac{4\omega_o \sin^2 \omega_o}{\sin 2\omega_o - 2\omega_o \cos 2\omega_o}. \tag{12}$$

Concerning the accuracy of the solution, it can be seen that by considering $R = (\alpha + b)/2 \ll R_O$ (or in other words that $R_O \to \infty$ in comparison with the major axis α of the elliptic hole) then indeed, $\varphi_*(\zeta) \to 0$ and $\psi_*(\zeta) \to 0$ for $\zeta \to \infty$. Therefore, the assumption that $\varphi(\zeta) \to \varphi_o(\zeta)$ and $\psi(\zeta) \to \psi_o(\zeta)$ on L_O is fulfilled. In other words, the ring's solution dominates at points far from L. Obviously, as L increases beyond certain limits (and therefore R becomes well comparable to R_O), the infinite-region assumption collapses. In such a case, the influence of L becomes stronger affecting also the region close to the disc's periphery L_O. An attempt to assess the degree of accuracy of the solution as well as the limits of its applicability is presented in Sect. 3.3 below, where the results for the SIFs (as obtained according to the present approach) are compared against the respective ones according to the widely accepted formulae for the SIFs introduced by Atkinson et al. [6] almost thirty years ago.

2.3 The displacement field along the boundary of the elliptic hole

Introducing now $\varphi(\zeta)$ and $\psi(\zeta)$, as they were obtained in Eqs. (9) and (10), into the well-known formula [8]

$$2\mu(u + iv) = \kappa\varphi(\zeta) - \frac{\omega(\zeta)}{\overline{\omega'(\zeta)}}\overline{\varphi'(\zeta)} - \overline{\psi(\zeta)}, \tag{13}$$

setting $\zeta = s = e^{i\theta}$ and separating real $\Re$ from imaginary $\Im$ parts, the Cartesian components of the displacements at any point on the elliptic hole's boundary L are obtained analytically as:

$$u_L(\theta) = \frac{P_c R(\kappa + 1)}{2\pi\mu} \left\{ \Re\left[(1 - m)b_0 - B_0' + R^2\left[\left(m - 1 - 2m^2\right)B_2 - mB_2'\right]\right]\cos\theta \right.$$

$$+ R^2 \Re\left[\left(\frac{1}{3} - m\right)B_2 - \frac{B_2'}{3}\right]\cos 3\theta + \Im\left[B_0' + R^2\left[\left(1 + 2m^2 - m\right)B_2 + mB_2'\right]\right]\sin\theta$$

$$- R^2 \Im\left[\left(\frac{1}{3} - m\right)B_2 - \frac{B_2'}{3}\right]\sin 3\theta + \sum_{n=1}^{\infty} R^{4n}\left[\Re B_{4n}\left(\frac{\Re G_{4n+1}^\infty(\theta)}{4n+1} - \Re G_{4n}^0(\theta)\right)\right.$$

$$- \Im B_{4n}\left(\frac{\Im G_{4n+1}^\infty(\theta)}{4n+1} + \Im G_{4n}^0(\theta)\right) - \frac{\Re B_{4n}'\Re G_{4n+1}^0(\theta) + \Im B_{4n}'\Im G_{4n+1}^0(\theta)}{4n+1}$$

$$+ R^2 \left(\Re B_{2(2n+1)} \left(\frac{\Re G^\infty_{4n+3}(\theta)}{4n+3} - \Re G^0_{2(2n+1)}(\theta) \right) - \Im B_{2(2n+1)} \left(\frac{\Im G^\infty_{4n+3}(\theta)}{4n+3} \right. \right.$$

$$\left. \left. + \Im G^0_{2(2n+1)}(\theta) \right) - \frac{\Re B'_{2(2n+1)} \Re G^0_{4n+3}(\theta) + \Im B'_{2(2n+1)} \Im G^0_{4n+3}(\theta)}{4n+3} \right) \right] \right\} , \tag{14}$$

$$v_L(\theta) = \frac{P_c R (\kappa + 1)}{2\pi\mu} \left\{ \Re \left[(1+m)b_0 + B'_0 + R^2 \left[(m+1+2m^2) B_2 + m B'_2 \right] \right] \sin\theta \right.$$

$$+ R^2 \Re \left[\left(\frac{1}{3} + m \right) B_2 + \frac{B'_2}{3} \right] \sin 3\theta + \Im \left[B'_0 + R^2 \left[(1+2m^2+m) B_2 + m B'_2 \right] \right] \cos\theta$$

$$+ R^2 \Im \left[\left(\frac{1}{3} + m \right) B_2 + \frac{B'_2}{3} \right] \cos 3\theta + \sum_{n=1}^\infty R^{4n} \left[\Im B_{4n} \left(\frac{\Re G^\infty_{4n+1}(\theta)}{4n+1} + \Re G^0_{4n}(\theta) \right) \right.$$

$$+ \Re B_{4n} \left(\frac{\Im G^\infty_{4n+1}(\theta)}{4n+1} - \Im G^0_{4n}(\theta) \right) + \frac{\Im B'_{4n} \Re G^0_{4n+1}(\theta) - \Re B'_{4n} \Im G^0_{4n+1}(\theta)}{4n+1}$$

$$+ R^2 \left(\Im B_{2(2n+1)} \left(\frac{\Re G^\infty_{4n+3}(\theta)}{4n+3} + \Re G^0_{2(2n+1)}(\theta) \right) + \Re B_{2(2n+1)} \left(\frac{\Im G^\infty_{4n+3}(\theta)}{4n+3} \right. \right.$$

$$\left. \left. \left. - \Im G^0_{2(2n+1)}(\theta) \right) + \frac{\Im B'_{2(2n+1)} \Re G^0_{4n+3}(\theta) - \Re B'_{2(2n+1)} \Im G^0_{4n+3}(\theta)}{4n+3} \right) \right] \right\} . \tag{15}$$

The real and imaginary parts of functions $G^\infty_j(\theta)$ and $G^0_j(\theta)$ (as obtained from the respective expressions of $G^\infty_j(\zeta)$ and $G^0_j(\zeta)$ given in "Appendix II") are included, again due to their lengthiness, in "Appendix III" (in the order they appear in Eqs. (14) and (15)).

2.4 The stress field in the elliptically perforated disc

The components of the stress field at any point of the elliptically perforated disc are obtained by taking advantage of the familiar formulae [8]:

$$\sigma_\rho - i\sigma_{\rho\theta} = 2\Re\Phi(\zeta) - \frac{\zeta^2}{\rho^2 \overline{\omega'(\zeta)}} \left[\overline{\omega(\zeta)} \Phi'(\zeta) + \omega'(\zeta)\Psi(\zeta) \right],$$

$$\sigma_\rho + \sigma_\theta = 4\Re\Phi(\zeta). \tag{16}$$

The functions $\Phi(\zeta) = \varphi'(\zeta)/\omega'(\zeta)$ and $\Psi(\zeta) = \psi'(\zeta)/\omega'(\zeta)$ are relatively easily obtained by combining Eqs. (4), (9) and (10).

Focusing attention to the points of the disc along the x-axis, the Cartesian components $\sigma_x (= \sigma_\rho)$, $\sigma_y (= \sigma_\theta)$ and $\sigma_{xy} (= \sigma_{\rho\theta})$ of the respective stress field are obtained as follows:

$$\left. \sigma_x \atop \sigma_y \right\} = \frac{2P_c}{\pi} \frac{\xi^2}{\xi^2 - m} \left\{ \Re \left(mB_2 + \frac{B'_2}{3} \right) \frac{3R^2}{\xi^4} + \frac{mb_0 + \Re B'_0 + R^2 \Re \left[(1+2m^2) B_2 + m B'_2 \right]}{\xi^2} \right.$$

$$+ R^2 \Re B_2 (m + \xi^2) + b_0 + \sum_{n=1}^\infty R^{4n} \left[\Re B_{4n} \left(\frac{1}{4n+1} \frac{\mathrm{d}G^\infty_{4n+1}}{\mathrm{d}\zeta}(\xi) - \frac{\mathrm{d}G^0_{4n}}{\mathrm{d}\zeta}(\xi) \right) - \frac{\Re B'_{4n}}{4n+1} \frac{\mathrm{d}G^0_{4n+1}}{\mathrm{d}\zeta}(\xi) \right.$$

$$\left. \left. + R^2 \left(\Re B_{2(2n+1)} \left(\frac{1}{4n+3} \frac{\mathrm{d}G^\infty_{4n+3}}{\mathrm{d}\zeta}(\xi) - \frac{\mathrm{d}G^0_{2(2n+1)}}{\mathrm{d}\zeta}(\xi) \right) - \frac{\Re B'_{2(2n+1)}}{4n+3} \frac{\mathrm{d}G^0_{4n+3}}{\mathrm{d}\zeta}(\xi) \right) \right] \right\}$$

$$\mp \frac{P_c}{\pi} \frac{\xi^2}{(\xi^2 - m)^3} \left\{ 3\Re B'_0 + R^2 \Re B_2 \left[m \left(\frac{6m^2 - 8m}{\xi^4} - \frac{6m - 13.33}{\xi^2} - 12 \right) + 4(1 + 3m^2) \right] \right.$$

$$\left. + R^2 \Re B'_2 \left(\frac{2m^2 - 3m}{\xi^4} - \frac{2m - 5}{\xi^2} + 6m - 4 \right) - \frac{m}{\xi^2} \Re \left[\frac{4 (1 + 3m^2) R^2 B_2}{3} + B'_0 + 2m R^2 B'_2 \right] \right.$$

$$+ R^2 \Re B_2' \left(\xi^6 - \frac{5m\xi^4}{3} \right) + \Re \left(B_0' + \frac{2mR^2 B_2'}{3} \right) (\xi^4 - 3m\xi^2) + 2R^2 \Re B_2 \left(\xi^6 - m\xi^4 - 3m^2\xi^2 - m^3 \right)$$

$$+ 2 \left(\xi^2 + m \right) \left[(1-m)^2 b_0 + R^2 \left(2m + 2m^3 - 2m^2 - 1 \right) \Re B_2 + (m-1) \left(\Re B_0' + mR^2 \Re B_2' \right) \right]$$

$$+ \left[m(1-2m) - m\xi^4 + \left(1 - 2m + 3m^2 \right) \xi^2 \right]$$

$$\cdot \sum_{n=1}^{\infty} R^{4n} \left[\Re B_{4n} \left(\frac{1}{4n+1} \frac{\mathrm{d}G_{4n+1}^{\infty}}{\mathrm{d}\zeta}(\xi) - \frac{\mathrm{d}G_{4n}^0}{\mathrm{d}\zeta}(\xi) \right) - \frac{\Re B_{4n}'}{4n+1} \frac{\mathrm{d}G_{4n+1}^0}{\mathrm{d}\zeta}(\xi) \right.$$

$$\left. + R^2 \left(\Re B_{2(2n+1)} \left(\frac{1}{4n+3} \frac{\mathrm{d}G_{4n+3}^{\infty}}{\mathrm{d}\zeta}(\xi) - \frac{\mathrm{d}G_{2(2n+1)}^0}{\mathrm{d}\zeta}(\xi) \right) - \frac{\Re B_{2(2n+1)}'}{4n+3} \frac{\mathrm{d}G_{4n+3}^0}{\mathrm{d}\zeta}(\xi) \right) \right]$$

$$+ \left[m(1-m)\xi - \left(1 - m^2 \right) \xi^3 + (1-m)\xi^5 \right]$$

$$\cdot \sum_{n=1}^{\infty} R^{4n} \left[\Re B_{4n} \left(\frac{1}{4n+1} \frac{d^2 G_{4n+1}^{\infty}}{d\zeta^2}(\xi) - \frac{d^2 G_{4n}^0}{d\zeta^2}(\xi) \right) - \frac{\Re B_{4n}'}{4n+1} \frac{d^2 G_{4n+1}^0}{d\zeta^2}(\xi) \right.$$

$$\left. + R^2 \left(\Re B_{2(2n+1)} \left(\frac{1}{4n+3} \frac{d^2 G_{4n+3}^{\infty}}{d\zeta^2}(\xi) - \frac{d^2 G_{2(2n+1)}^0}{d\zeta^2}(\xi) \right) - \frac{\Re B_{2(2n+1)}'}{4n+3} \frac{d^2 G_{4n+3}^0}{d\zeta^2}(\xi) \right) \right]$$

$$+ (m - \xi^2)^2 \cdot \sum_{n=1}^{\infty} R^{4n} \left[\Re B_{4n} \left(\frac{\mathrm{d}G_{4n}^{\infty}}{\mathrm{d}\zeta}(\xi) - \frac{1}{4n+1} \frac{\mathrm{d}G_{4n+1}^0}{\mathrm{d}\zeta}(\xi) \right) + \frac{\Re B_{4n}'}{4n+1} \frac{\mathrm{d}G_{4n+1}^{\infty}}{\mathrm{d}\zeta}(\xi) \right.$$

$$\left. \left. + R^2 \left(\Re B_{2(2n+1)} \left(\frac{\mathrm{d}G_{2(2n+1)}^{\infty}}{\mathrm{d}\zeta}(\xi) - \frac{1}{4n+3} \frac{\mathrm{d}G_{4n+3}^0}{\mathrm{d}\zeta}(\xi) \right) + \frac{\Re B_{2(2n+1)}'}{4n+3} \frac{\mathrm{d}G_{4n+3}^{\infty}}{\mathrm{d}\zeta}(\xi) \right) \right] \right\}, \quad (17)$$

$$\sigma_{xy} = \frac{P_c}{\pi} \frac{\xi^2}{(\xi^2 - m)^3} \left\{ -3\Im B_0' - R^2 \Im B_2 \left[m \left(\frac{6m^2 - 8m}{\xi^4} - \frac{6m - 13.33}{\xi^2} - 12 \right) + 4 \left(1 + 3m^2 \right) \right] \right.$$

$$- R^2 \Im B_2' \left(\frac{2m^2 - 3m}{\xi^4} - \frac{2m - 5}{\xi^2} + 6m - 4 \right) + \frac{m}{\xi^2} \Im \left[\frac{4 \left(1 + 3m^2 \right) R^2 B_2}{3} + B_0' + 2mR^2 B_2' \right]$$

$$+ R^2 \Im B_2' \left(\xi^6 - \frac{5m\xi^4}{3} \right) + \Im \left(B_0' + \frac{2mR^2 B_2'}{3} \right) (\xi^4 - 3m\xi^2) + 2R^2 \Im B_2 \left(\xi^6 - m\xi^4 - 3m^2\xi^2 - m^3 \right)$$

$$+ 2(\xi^2 + m) \Im \left[R^2 \left(1 + 2m^2 \right) B_2 + B_0' + mR^2 B_2' \right] + \left[m(1-2m) - m\xi^4 + \left(1 - 2m + 3m^2 \right) \xi^2 \right]$$

$$\cdot \sum_{n=1}^{\infty} R^{4n} \left[\Im B_{4n} \left(\frac{1}{4n+1} \frac{\mathrm{d}G_{4n+1}^{\infty}}{\mathrm{d}\zeta}(\xi) + \frac{\mathrm{d}G_{4n}^0}{\mathrm{d}\zeta}(\xi) \right) + \frac{\Im B_{4n}'}{4n+1} \frac{\mathrm{d}G_{4n+1}^0}{\mathrm{d}\zeta}(\xi) \right.$$

$$\left. + R^2 \left(\Im B_{2(2n+1)} \left(\frac{1}{4n+3} \frac{\mathrm{d}G_{4n+3}^{\infty}}{\mathrm{d}\zeta}(\xi) + \frac{\mathrm{d}G_{2(2n+1)}^0}{\mathrm{d}\zeta}(\xi) \right) + \frac{\Im B_{2(2n+1)}'}{4n+3} \frac{\mathrm{d}G_{4n+3}^0}{\mathrm{d}\zeta}(\xi) \right) \right]$$

$$+ \left[m(1-m)\xi - (1-m^2)\xi^3 + (1-m)\xi^5 \right]$$

$$\cdot \sum_{n=1}^{\infty} R^{4n} \left[\Im B_{4n} \left(\frac{1}{4n+1} \frac{d^2 G_{4n+1}^{\infty}}{d\zeta^2}(\xi) + \frac{d^2 G_{4n}^0}{d\zeta^2}(\xi) \right) + \frac{\Im B_{4n}'}{4n+1} \frac{d^2 G_{4n+1}^0}{d\zeta^2}(\xi) \right.$$

$$\left. + R^2 \left(\Im B_{2(2n+1)} \left(\frac{1}{4n+3} \frac{d^2 G_{4n+3}^{\infty}}{d\zeta^2}(\xi) + \frac{d^2 G_{2(2n+1)}^0}{d\zeta^2}(\xi) \right) + \frac{\Im B_{2(2n+1)}'}{4n+3} \frac{d^2 G_{4n+3}^0}{d\zeta^2}(\xi) \right) \right]$$

$$+ \left(m - \xi^2 \right)^2 \cdot \sum_{n=1}^{\infty} R^{4n} \left[\Im B_{4n} \left(\frac{\mathrm{d}G_{4n}^{\infty}}{\mathrm{d}\zeta}(\xi) + \frac{1}{4n+1} \frac{\mathrm{d}G_{4n+1}^0}{\mathrm{d}\zeta}(\xi) \right) + \frac{\Im B_{4n}'}{4n+1} \frac{\mathrm{d}G_{4n+1}^{\infty}}{\mathrm{d}\zeta}(\xi) \right.$$

$$+R^2 \left(\Im B_{2(2n+1)} \left(\frac{dG_{2(2n+1)}^{\infty}}{d\zeta}(\xi) + \frac{1}{4n+3} \frac{dG_{4n+3}^{0}}{d\zeta}(\xi) \right) + \frac{\Im B_{2(2n+1)}'}{4n+3} \frac{dG_{4n+3}^{\infty}}{d\zeta}(\xi) \right) \right] \right\}. \quad (18)$$

In Eqs. (17) and (18), $G_j^{\infty}(\xi)$ and $G_j^{0}(\xi)$ are provided by the expressions of "Appendix II" by simply setting $\zeta = \xi$. In addition, $\frac{dG_j^{\infty}}{d\zeta}(\xi)$, $\frac{dG_j^{0}}{d\zeta}(\xi)$ and $\frac{d^2 G_j^{\infty}}{d\zeta^2}(\xi)$, $\frac{d^2 G_j^{0}}{d\zeta^2}(\xi)$ are the first and second-order derivatives of $G_j^{\infty}(\zeta)$, $G_j^{0}(\zeta)$ with respect to ζ at the point $\zeta = \xi$. Regarding the value of ξ, inverting the conformal mapping (Eq. (4)) it follows that

$$\xi = \left(x + \sqrt{x^2 - 4mR^2} \right) \Big/ (2R).$$

2.5 Applications demonstrating the capabilities of the solution

In order for the capabilities of the solution introduced in Sects. 2.3 and 2.4 to become clear, and also for a quantitative overview of the variation of the displacement and stress components along some characteristic loci to be obtained, a specific case is here considered: the disc's radius R_O is equal to 0.05 m and its thickness t is equal to 0.01 m. The axes of the elliptic hole are $\alpha = 0.4R_O = 0.02$ m and $b = 0.1R_O = 0.005$ m, i.e. the ratio α/b is equal to 4. The disc is assumed to be made of PMMA with Young's modulus $E = 3.19$ GPa and Poisson's ratio $v = 0.36$. The disc is squeezed between the jaws of the ISRM-suggested device for the standardized implementation of the Brazilian-disc test, which are made of steel with Young's modulus $E_J = 210$ GPa and Poisson's ratio $v_J = 0.30$. The externally imposed load P_{frame} is considered equal to 20 kN. The solution of the respective contact problem yields for the contact semi-angle $\omega_o = 11.88°$ (see the first of Eqs. (11)). The number of additional terms, n, used ranges from about 4 to 20, depending on whether displacements along L or stresses along the x-axis are considered, according to a preliminary convergence analysis which indicated that beyond these values any additional terms do not contribute significantly to the accuracy of the results obtained.

As far as it concerns the orientation ϕ_o of the long semi-axis of the elliptic hole with respect to the symmetry axis of the pressure distribution, two configurations were considered: one with $\phi_o = 0°$ (absolutely symmetric) and one with $\phi_o = 30°$. The first one is of crucial practical importance since the limiting value of the transverse normal stress $\sigma_y(y = 0)$ along this locus is used as an alternative approach for the determination of the stress intensity factors (SIFs) [17] (assuming that the elliptic hole tends to a mathematic crack). The second one is considered since previous studies [5,6] indicate that (for short mathematic cracks) it is approximately equal to the limiting value beyond which K_I becomes negative. Moreover, it offers an overview of the potentials of the present approach even in case the symmetry of the load with respect to the elliptic hole is violated. For all the calculations following the commercially available software, Wolfram Mathematica 10 was used.

In Fig. 3, the polar variation of the displacements of the elliptic hole's upper lip is plotted against the angle θ (considered in the ζ plane) within the interval $[0°, 180°]$. As it is expected, for $\phi_o = 0°$ (Fig. 3a), v_L is symmetric whereas u_L is anti-symmetric with respect to the $\theta = 90°$ line. In other words, the shape of the hole remains elliptic, the length of its long semi-axis decreases while that of the short one increases. The maximum value of the u_L-component is equal to about 0.021α or equivalently to about 0.42 mm. For the v_L-component, the maximum value is equal to 0.011α or equivalently to about 0.21 mm.

On the other hand, for $\phi_o = 30°$ (Fig. 3b), the symmetry of the displacements is lost and the deformed shape of the hole is not anymore elliptic. It is observed that now the values of the v_L-component are not constantly positive: a sign change occurs at an angle equal to about $\theta = 85°$. The maximum absolute value detected at $\theta = 0°$ and $180°$ is equal to about 0.015α or equivalently to 0.30 mm. For the u_L-component, the maximum absolute value attained at an angle θ equal to about $56°$, is equal to about 0.019α or equivalently to about 0.38 mm. In addition, it is mentioned that the axes of the ellipse are slightly rotated with respect to their initial orientation. The specific point will be discussed again in Sect. 5 in conjunction to the partial contact of the crack lips observed for specific combinations of ϕ_o and P_{frame}.

The results concerning the stress field are plotted in Fig. 4a, b. As it can be seen from Fig. 4a, in case $\phi_o = 0°$, σ_x is of compressive nature almost all along the locus considered ($\alpha < x < R_O$) and only as $x \to \alpha$ it becomes tensile. Its magnitude reaches $-P_c$ for $x \to R_O$, while its maximum tensile value attained at $x \to \alpha$ is equal to only $0.14P_c$. From the same figure, it is seen that σ_y is compressive in the $0.78R_O \leq x \leq R_O$ range while in the $\alpha \leq x < 0.78R_O$ one it becomes tensile. Its magnitude ranges from $-P_c$ (at $x = R_O$) to $1.15P_c$ (at $x = \alpha$). What's more, σ_{xy} is zero due to the symmetry of the configuration. In case the loading symmetry
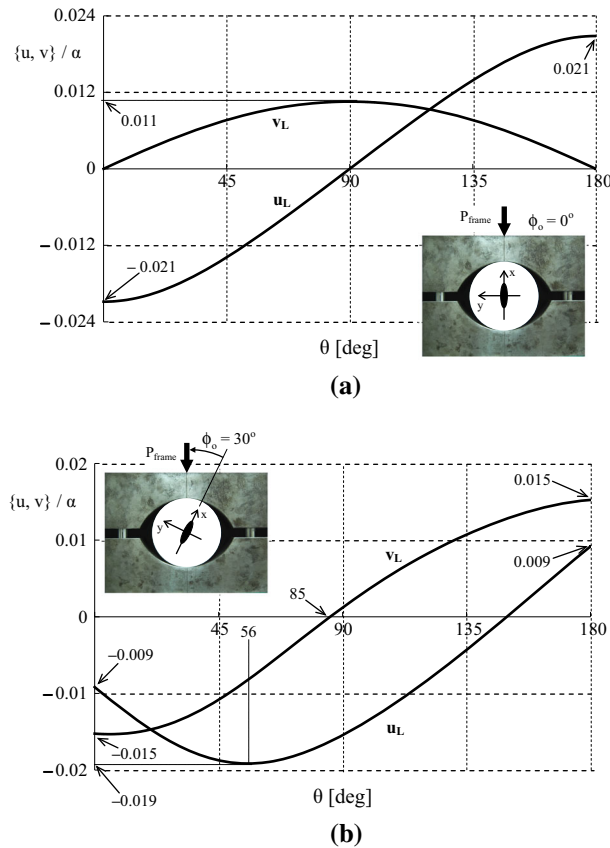
Fig. 3 The variation of the displacement components along the upper arc of the elliptic hole for $\phi_o = 0°$ (**a**) and $\phi_o = 30°$ (**b**)

axis is inclined with respect to the hole's long semi-axis ($\phi_o = 30°$), it is seen from Fig. 4b that all three stress components are negative almost all along the locus studied ($\alpha \leq x \leq R_O$). As it is expected, their magnitude tends to zero as $x \rightarrow R_O$, while it reaches minimum values equal to about $-0.16P_c$ at $x = \alpha$ and $x = 0.70R_O$ (for σ_y), $-0.38P_c$ at $x = 0.44R_O$ (for σ_{xy}) and $-0.08P_c$ at $x = 0.50R_O$ (for σ_x).

It is indicated at this point that for $x = R_O$, i.e. on the discs' outer periphery, the boundary conditions $\sigma_x = \sigma_y = \sigma_{xy} = 0$ (stress-free external boundary) are only approximately satisfied, especially concerning the $\sigma_{xy}(x = R_O) = 0$ condition. This behaviour is a consequence of series truncation errors together with the limited accuracy of the infinite-region assumption (when the elliptic hole's major axis exceeds 80 % of the disc's radius) in case of asymmetric configurations (as it is the one here considered ($\phi_o = 30°$)). Regarding the last statement, it is recalled that stresses along the elliptically perforated disc's periphery should by assumption approximate those of the respective ring. Indeed, as it is seen from Fig. 4c, where the stress fields of the disc with the elliptic hole and of the respective ring are drawn in juxtaposition to each other, the normal stresses are very much alike at the point $x = R_O$ (the same number n of additional terms has been considered for both solutions). This is not the case for the shear stress for which a slight difference appears. However, this difference should be expected given that in case $\phi_o \neq 0°$ and $\phi_o \neq 90°$, the inherent asymmetry of the configuration does not permit static equilibrium to be maintained unless a distribution of shear stresses is considered (along the disc's boundary), maintaining equilibrium by counterbalancing the inevitable rigid-body-rotation tendency. Such a distribution of shear stresses was not taken into account (according to the common procedure of almost all existing analytic approaches [6]) in the formulation of the problem. This point will be further discussed in Sect. 4. In any case, the relatively small magnitude of this inconsistency and also the fact that emphasis will be paid exclusively in the disc's area around the tips of the elliptic hole rather than along its periphery, render the specific discrepancies well manageable.

Consider now that for the specific configuration with $\phi_o = 0°$, the short semi-axis of the elliptic hole is becoming gradually shorter and shorter while the numerical values of the other quantities previously adopted are kept constant. Clearly, the σ_y-stress component increases due to the intensification of the stress concentration.
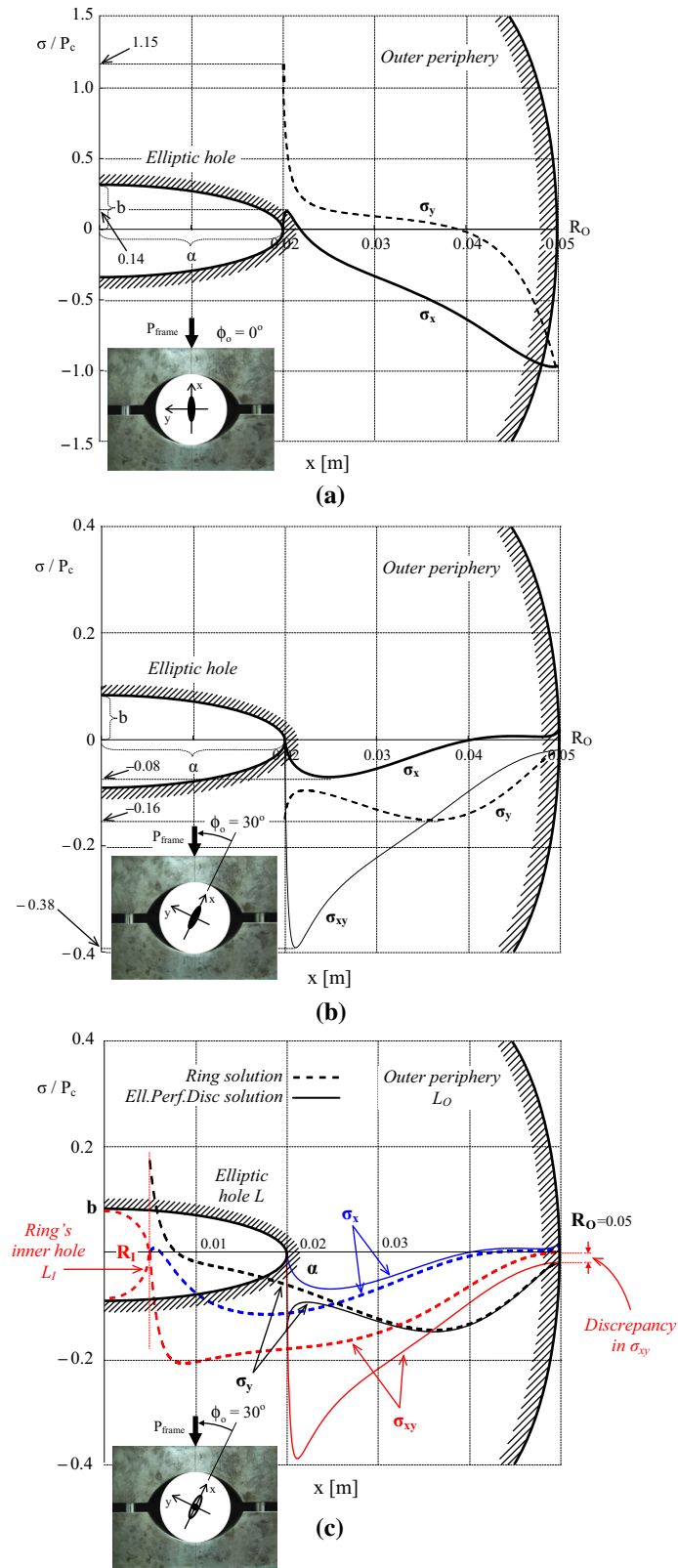
Fig. 4 The variation of the stress components along the positive *x*-axis for $\phi_o = 0°$ (**a**) and $\phi_o = 30°$ (**b**). The stress field in the circular ring along the same as above locus in juxtaposition to the stress field in the respective elliptically perforated disc for $\phi_o = 30°$ (**c**)
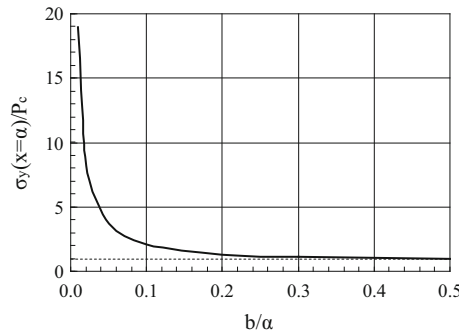
Fig. 5 The stress concentration at the hole's tips for $\phi_o = 0°$ against the ratio of the elliptic hole's semi-axes

To quantify this increase, the value of σ_y normalized over P_c at $x = \alpha$ is plotted against the b/α ratio in Fig. 5. As it is expected, for relatively increased b/α ratios (exceeding 0.2), the magnitude of $\sigma_y(x = \alpha)$ is more or less insensitive to the exact b/α value. In particular, for b/α exceeding 0.5 its value tends to P_c. On the other hand, as b/α becomes small $\sigma_y(x = \alpha)$ starts increasing abruptly. It is mentioned characteristically that for $b/\alpha = 0.01$ $\sigma_y(x = \alpha)$ is almost twenty times the value of P_c. For b/α ratios even smaller than 0.01, the value of $\sigma_y(x = \alpha)$ tends to infinity, as it is obviously expected (recall that the analysis described in the present study is based on the linear elasticity assumption), since the elliptic hole tends to become a mathematic crack of zero distance between its lips, and therefore the "stress concentration" concept gives its position to the concept of " stress intensity". The specific limiting case (i.e. $b/\alpha \to 0$) is the object of next Sect. 3, where the stress intensity factors will be determined.

At any other arbitrary point of the elliptically perforated disc, the stress field can be obtained similarly by substituting in Eqs. (16) the expressions for the complex potentials (Eqs. (9) and (10)). Since the respective expressions are extremely lengthy (and considering that from here on attention will be focused at points along x-axis), they are omitted.

3 The stress intensity factors (SIFs)

As it was previously mentioned, the case with $b/\alpha \to 0$ corresponds to the circular disc with a central discontinuity which closely resembles the circular disc with a central mathematic crack of length 2α. This configuration is of crucial importance for practical applications since it simulates the familiar cracked Brazilian-disc test, which is widely used for the determination of mode-I fracture toughness of brittle geomaterials.

The respective stress and displacement fields for this limiting case are obtained by setting $b = R_I = 0$, so that $m = 1$ and $R = \alpha/2$ in the corresponding formulae of Sect. 2, which are still valid. For obvious reasons (linear elasticity), the theoretical solution provides singular stresses at the points $\pm\alpha$ (standing now as the tips of a mathematic crack) that are conveniently expressed with the aid of the respective stress intensity factors [17].

3.1 The analytic expressions for the SIFs according to the present approach

The SIFs are usually determined either from the stress field or through the complex potential $\Phi(z)$ [17]. The latter is the alternative chosen for the needs of the present study. In this direction, it is recalled that $\Phi(\zeta) = \varphi'(\zeta)/\omega'(\zeta)$. Then, reverting to the variable z, through the inversion of Eq. (4), i.e. by writing $\zeta = \left(z + \sqrt{z^2 - 4mR^2}\right)/(2R)$, and by considering $R = \alpha/2$ and $m = 1$, which is the case when the minor axis of the elliptic hole b is zeroed, $\Phi(z)$ is obtained in the case the elliptic hole has become a crack of length 2α, as:

$$\Phi(z) = \frac{P_c}{\pi} \frac{\left(z + \sqrt{z^2 - \alpha^2}\right)^2}{\left(z + \sqrt{z^2 - \alpha^2}\right)^2 - \alpha^2} \left\{ \mathsf{b}_0 + \frac{\mathsf{B}_2}{4} \left[\alpha^2 + \left(z + \sqrt{z^2 - \alpha^2}\right)^2\right] \right.$$

$$+ \frac{\mathsf{b}_0 + \overline{\mathsf{B}_0'} + \frac{\alpha^2}{4}\left(3\overline{\mathsf{B}_2} + \overline{\mathsf{B}_2'}\right)}{\left(z + \sqrt{z^2 - \alpha^2}\right)^2} \alpha^2 + \left(\overline{\mathsf{B}_2} + \frac{\overline{\mathsf{B}_2'}}{3}\right) \frac{3\alpha^6}{4\left(z + \sqrt{z^2 - \alpha^2}\right)^4}$$

$$+ \sum_{n=1}^{\infty} \left(\frac{\alpha}{2}\right)^{4n} \left[\frac{\mathsf{B}_{4n}}{4n+1} \frac{\mathrm{d}G_{4n+1}^{\infty}}{\mathrm{d}\zeta}(z) - \overline{\mathsf{B}_{4n}} \frac{\mathrm{d}G_{4n}^0}{\mathrm{d}\zeta}(z) - \frac{\overline{\mathsf{B}_{4n}'}}{4n+1} \frac{\mathrm{d}G_{4n+1}^0}{\mathrm{d}\zeta}(z)\right.$$

$$\left.\left. + \frac{\alpha^2}{4} \left(\frac{\mathsf{B}_{2(2n+1)}}{4n+3} \frac{\mathrm{d}G_{4n+3}^{\infty}}{\mathrm{d}\zeta}(z) - \overline{\mathsf{B}_{2(2n+1)}} \frac{\mathrm{d}G_{2(2n+1)}^0}{\mathrm{d}\zeta}(z) - \frac{\overline{\mathsf{B}_{2(2n+1)}'}}{4n+3} \frac{\mathrm{d}G_{4n+3}^0}{\mathrm{d}\zeta}(z)\right)\right]\right\}, \quad (19)$$

where b_0, B_j and B_j' denote the values of b_0, B_j and B_j' for $b = R_I = 0$, respectively. Their explicit expressions are given, again for brevity, in "Appendix IV". In addition, $\frac{\mathrm{d}G_j^{\infty}}{\mathrm{d}\zeta}(z)$ and $\frac{\mathrm{d}G_j^0}{\mathrm{d}\zeta}(z)$ are the first-order derivatives of $G_j^{\infty}(\zeta)$ and $G_j^0(\zeta)$ with respect to ζ, after reverting to the variable z. Clearly, $\Phi(z)$ as it has been obtained in Eq. (19) is singular at the crack tips $\pm\alpha$. It is easily seen that in order to remove the singularity from $\Phi(z)$ at points $\pm\alpha$, passing instead to the notion of SIFs, the later must be redefined in the case of an elliptic hole as:

$$K_I = 2\sqrt{\frac{\pi}{\alpha}} \cdot \Re \left\{\lim_{z \to \alpha} \left[\left(z + \sqrt{z^2 - \alpha^2} - \alpha\right) \Phi(z)\right]\right\},$$

$$K_{II} = -2\sqrt{\frac{\pi}{\alpha}} \cdot \Im \left\{\lim_{z \to \alpha} \left[\left(z + \sqrt{z^2 - \alpha^2} - \alpha\right) \Phi(z)\right]\right\}. \quad (20)$$

Combination of Eqs. (19) and (20) yields:

$$K_I = P_c \sqrt{\frac{\alpha}{\pi}} \left\{2\mathsf{b}_0 + \Re\mathsf{B}_0' + 2\alpha^2\left(\Re\mathsf{B}_2 + \frac{\Re\mathsf{B}_2'}{4}\right) + \sum_{n=1}^{\infty} \left(\frac{\alpha}{2}\right)^{4n}\left[\Re\mathsf{B}_{4n}\left(\frac{\mathsf{G}_{4n+1}^{\infty}}{4n+1} - \mathsf{G}_{4n}^0\right)\right.\right.$$

$$\left.\left. - \frac{\Re\mathsf{B}_{4n}'}{4n+1}\mathsf{G}_{4n+1}^0 + \frac{\alpha^2}{4}\left(\Re\mathsf{B}_{2(2n+1)}\left(\frac{\mathsf{G}_{4n+3}^{\infty}}{4n+3} - \mathsf{G}_{2(2n+1)}^0\right) - \frac{\Re\mathsf{B}_{2(2n+1)}'}{4n+3}\mathsf{G}_{4n+3}^0\right)\right]\right\}, \quad (21)$$

$$K_{II} = P_c \sqrt{\frac{\alpha}{\pi}} \left\{\Im\mathsf{B}_0' + \alpha^2\left(\Im\mathsf{B}_2 + \frac{\Im\mathsf{B}_2'}{2}\right) - \sum_{n=1}^{\infty} \left(\frac{\alpha}{2}\right)^{4n}\left[\Im\mathsf{B}_{4n}\left(\frac{\mathsf{G}_{4n+1}^{\infty}}{4n+1} + \mathsf{G}_{4n}^0\right)\right.\right.$$

$$\left.\left. + \frac{\Im\mathsf{B}_{4n}'}{4n+1}\mathsf{G}_{4n+1}^0 + \frac{\alpha^2}{4}\left(\Im\mathsf{B}_{2(2n+1)}\left(\frac{\mathsf{G}_{4n+3}^{\infty}}{4n+3} + \mathsf{G}_{2(2n+1)}^0\right) + \frac{\Im\mathsf{B}_{2(2n+1)}'}{4n+3}\mathsf{G}_{4n+3}^0\right)\right]\right\}, \quad (22)$$

where G_j^0, G_j^{∞} are real quantities obtained from $\frac{\mathrm{d}G_j^{\infty}}{\mathrm{d}\zeta}(z)$, $\frac{\mathrm{d}G_j^0}{\mathrm{d}\zeta}(z)$ for $z = \alpha$ (or for $\zeta = 1$) and $m = 1$. Their analytic expressions are included in "Appendix V".

3.2 The influence of critical geometric features on the values of the SIFs

Taking now advantage of the analytic expressions derived in Sect. 3.1, it is possible to explore in a quantitative manner the role of some critical geometrical parameters of the overall configuration on the values of the SIFs.

As a first step in this direction, the mode-I and mode-II SIFs are plotted in Fig. 6 against the inclination, ϕ_o, of the crack axis with respect to the symmetry axis of the pressure distribution. The disc's radius R_O is again equal to $0.05\,\text{m}$, and its thickness t is equal to $0.01\,\text{m}$. A relatively long crack with $2\alpha = R_O$ is considered, while four different (arbitrarily prescribed) values are ascribed to the contact semi-angle ω_o, equal to $1°$ (approaching the point force loading type), $10°$, $20°$ and $30°$. The overall external force P_{frame} is assumed equal to $20\,\text{kN}$, and the respective P_c values are obtained through Eq. (12). The number n of additional terms of the series
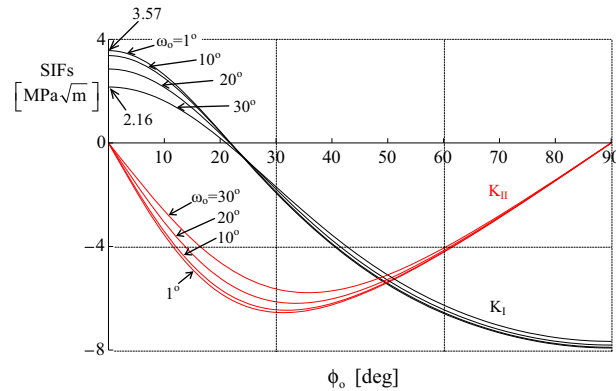
Fig. 6 The variation of the mode-I and mode-II SIFs versus the inclination of the crack axis for various lengths of the contact arc

expansion used here is restricted to 3, since convergence analysis indicated that increasing n further does not contribute to the accuracy of the solution.

It is seen from Fig. 6 that for relatively small ϕ_o values, the mode-I SIF is positive indicating a tendency of the stress field to open the crack. However, at some critical angle $\phi_{o,\mathrm{cr}}$ (the exact value of which depends—very slightly—on the contact semi-angle ω_o), K_I is zeroed and becomes negative. The range of validity of the present analysis (and of any other similar one) is restricted in the $0 \leq \phi_o < \phi_{o,\mathrm{cr}}$ domain since negative K_I-values imply that the crack lips came in contact to each other and contact stresses have inevitably been generated. The appearance of contact stresses alters the initially considered boundary conditions (stress-free crack lips) rendering the solution in the $\phi_{o,\mathrm{cr}} \leq \phi_o \leq 90°$ domain unnatural (formalistic application of the respective formulae for the displacement field leads to overlapped crack lips as in the case of the infinite cracked plate [18,19]). The solution of the specific problem is very complicated for a crack in a finite domain. A relatively simple case of a finite circular domain with a short central crack was recently discussed by Markides et al. [20,21].

Concerning the mode-II SIF, it is seen from Fig. 6 that it is of constantly negative sign. Its magnitude increases with increasing ϕ_o for the whole range of ϕ_o values for which the present analysis is valid ($0 \leq \phi_o < \phi_{o,\mathrm{cr}}$).

From Fig. 6, it is also concluded that in general the values of both K_I and K_II do depend on the contact semi-angle ω_o. For K_I, this dependence is more pronounced for small ϕ_o-values and it is maximized at $\phi_o = 0°$. On the contrary, for K_II, this dependence is maximized at $\phi_o = \phi_{o,\mathrm{cr}}$. It is noticed, however, that for moderate ω_o-values (ranging from 0° to about 12.5°), this dependence is rather ignorable for practical applications. This is an interesting observation since it is by no means expected that the contact angle $2\omega_o$ could exceed 25° [22,23] in case a cracked disc made of a brittle geomaterial is compressed according to the ISRM standards [1,15]. It is therefore concluded that the simplified expressions used for the determination of fracture toughness according to the respective standards, which assume a small (arbitrarily determined) contact angle, are valid and the error due to the deformability of the disc–jaw elastic system could be ignored at least in a first approximation.

The second geometric parameter of interest is the disc's thickness. Its influence (for the same numerical data as before) is visualized in Fig. 7a, b for the PMMA–steel pair of disc's and jaw's materials. The number n of additional terms of the series expansion used is restricted again to three and the externally imposed load P_{frame} is kept constant equal to 20 kN. For thin discs, corresponding to the plane stress configuration, five cases are considered for the thickness t of the disc, equal to 0.002, 0.004, 0.006, 0.008 and 0.01 m. Following Muskhelishvili's [8] notation constant κ^* for plane stress conditions is equal to $(3 - \nu)/(1 + \nu)$. For disc thicknesses t exceeding 0.01 m, the problem is assumed to be a plane strain one and then Muskhelishvili's constant κ is equal to $3 - 4\nu$. For both plane stress and plane strain conditions, the contact semi-angle ω_o and the load parameter P_c are obtained from the respective contact problem according to Eq. (11). Therefore, all constants b_0 and B_j, B'_j appearing in the solution are functions of ω_o.

The variation of the mode-I and mode-II SIFs against the crack inclination angle ϕ_o is plotted in Fig. 7a. As it is expected, the magnitude of both K_I and K_II decreases with increasing thickness (recall that the external load is kept constant), tending to the respective plane strain distributions. It is seen that for $t = 0.01$ m, the plane stress distribution approaches accurately enough the respective plane strain one indicating that the specific thickness is the critical (limiting) value of the disc's thickness signalling the transition from plane
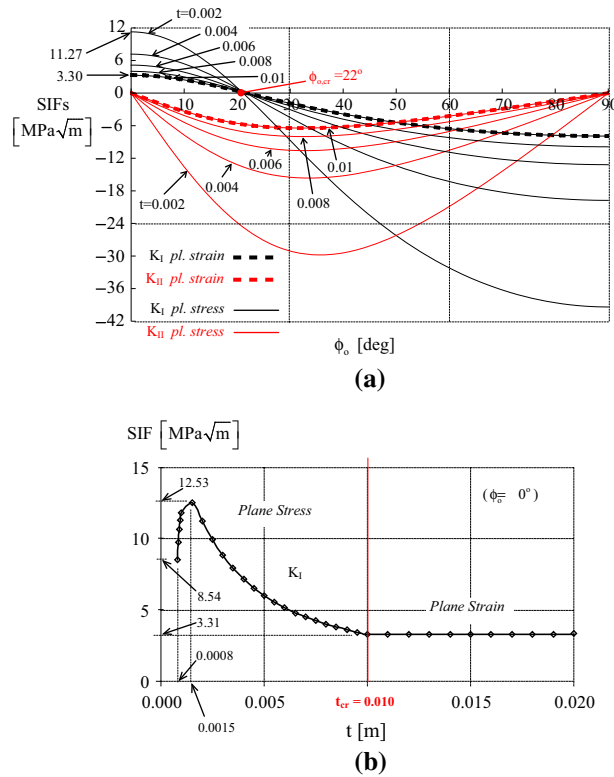
Fig. 7 a The dependence of the SIFs on the thickness of the disc. **b** The mode-I SIF against the disc thickness for $\phi_o = 0°$ for plane stress and plane strain conditions

stress to plane strain. Obviously, this limiting thickness value is not a universal constant since it depends on the level of the externally applied load.

From the same Fig. 7a, it is seen that the critical value of the crack inclination angle $\phi_{o,\mathrm{cr}}$, designating the end of the validity range of the analytic solution, does not depend on the disc's thickness. For the numerical values here assigned to the various parameters of the problem it holds that $\phi_{o,\mathrm{cr}} = 22°$.

The dependence of mode-I SIF on the disc's thickness for the specific case with $\phi_o = 0°$ (i.e. the configuration used for the determination of the mode-I fracture toughness K_{IC}) is plotted in Fig. 7b. It is observed that the $K_{\mathrm{I}} - t$ relation is not monotonous. A clear maximum appears at $t = 0.0015$ m. From this value, the K_{I}-values decrease smoothly tending to the respective plane strain value at about $t = 0.01$ m. Assuming that the load imposed is the one causing crack initiation, the plane strain value of K_{I} corresponds to the fracture toughness value which is considered as a material property somehow quantifying the resistance of the disc's material to crack propagation. It is mentioned at this point that the above results are of limited practical importance in case of very thin discs: imposing compressive load on very thin discs is very difficult (if not impossible) due to the inevitable buckling of the disc.

The last geometric parameter studied is the relative length of the crack with respect to the disc radius (the accuracy of the present solution for long cracks will be assessed in the next section). The specific parameter is of crucial importance since most analytic solutions are restricted to short cracks. The dependence of both K_{I} and K_{II} on ϕ_o is plotted in Fig. 8 for various α/R_O ratios ranging from very short cracks ($\alpha/R_O = 0.1$) to rather long ones ($\alpha/R_O = 0.5$). As it is expected, for $\phi_o = 0$, the mode-I SIF increases with increasing α/R_O ratios (from 1.5 for $\alpha/R_O = 0.1$ to 3.3 for $\alpha/R_O = 0.5$). For increasing crack inclination angles ϕ_o, the magnitude of K_{I} decreases, and this decrease is more abrupt for high α/R_O ratios. As a result, the angle ϕ_o, at which K_{I} becomes zero is equal to $\phi_{o,\mathrm{cr}} = 21.8°$ for $\alpha/R_O = 0.5$, while for $\alpha/R_O = 0.1$ it is equal to $\phi_{o,\mathrm{cr}} = 29.4°$. On the contrary, the dependence of K_{II} on α/R_O is more straightforward: increasing the ratio α/R_O the value of K_{II} decreases systematically at least for the range of ϕ_o values for which the present analytic solution is naturally sound ($0 \leq \phi_o < \phi_{o,\mathrm{cr}}$).
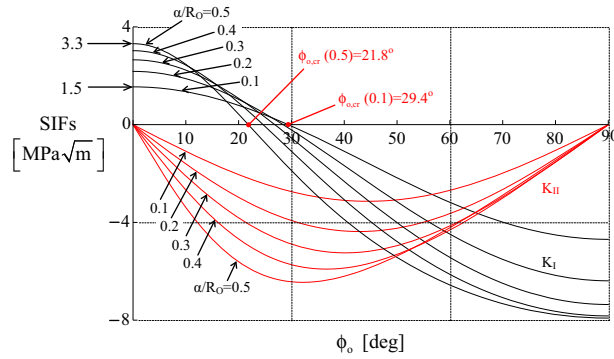
Fig. 8 The variation of the mode-I and mode-II SIFs versus the inclination of the crack axis for various crack lengths

3.3 Validation of the solution for the SIFs

In order for the above-described analytic solution to be properly validated, it is recalled that according to the pioneering paper by Atkinson et al. [6], the SIFs are given (adopting the notation of the present study) as:

$$K_I^{Atk} = \frac{P_{\text{frame}}}{R_O t} \sqrt{\frac{\alpha}{\pi}} \cdot \underbrace{\sum_{\ell=1}^{n} T_\ell \left(\frac{\alpha}{R_O}\right)^{2\ell-2} \mathcal{A}_\ell(\vartheta)}_{N_I}, \tag{23}$$

$$K_{II}^{Atk} = \frac{P_{\text{frame}}}{R_O t} \sqrt{\frac{\alpha}{\pi}} \cdot \underbrace{2 \sin 2\vartheta \sum_{\ell=1}^{n} S_\ell \left(\frac{\alpha}{R_O}\right)^{2\ell-2} \mathcal{B}_\ell(\vartheta)}_{N_{II}}. \tag{24}$$

In Eqs. (23) and (24), T_ℓ, S_ℓ, $\mathcal{A}_\ell(\vartheta)$ and $\mathcal{B}_\ell(\vartheta)$ are quantities provided by Atkinson et al. [6] in tabulated form. In fact, T_ℓ and S_ℓ are real coefficients related to the α/R_O ratio while $\mathcal{A}_\ell(\vartheta)$ and $\mathcal{B}_\ell(\vartheta)$ are sums involving angle ϑ, which according to the notation and terminology of the present study is equal to $\pi - \phi_o$.

On the other hand, considering (for comparison reasons) the case when the angle ω_o is arbitrarily prescribed, so that P_c is given by Eq. (12), the respective formulae of the present analysis (given by Eqs. (21) and (22)), are equivalently re-written as:

$$K_I = \frac{P_{\text{frame}}}{R_O t} \sqrt{\frac{\alpha}{\pi}} \cdot \underbrace{\left(\begin{array}{l} \frac{2\sin^2\omega_o}{\sin 2\omega_o - 2\omega_o \cos 2\omega_o} \left\{ 2b_0 + \Re B_0' + 2\alpha^2 \left(\Re B_2 + \frac{\Re B_2'}{4} \right) \right. \\ + \sum_{n=1}^{\infty} \left(\frac{\alpha}{2}\right)^{4n} \left[\Re B_{4n} \left(\frac{G_{4n+1}^{\infty}}{4n+1} - G_{4n}^0 \right) - \frac{\Re B_{4n}'}{4n+1} G_{4n+1}^0 \right. \\ \left. \left. + \frac{\alpha^2}{4} \left(\Re B_{2(2n+1)} \left(\frac{G_{4n+3}^{\infty}}{4n+3} - G_{2(2n+1)}^0 \right) - \frac{\Re B_{2(2n+1)}'}{4n+3} G_{4n+3}^0 \right) \right] \right\} \end{array} \right)}_{F_I}, \tag{25}$$

$$K_{II} = \frac{P_{\text{frame}}}{R_O t} \sqrt{\frac{\alpha}{\pi}} \cdot \underbrace{\left(\begin{array}{l} \frac{2\sin^2\omega_o}{\sin 2\omega_o - 2\omega_o \cos 2\omega_o} \left\{ \Im B_0' + \alpha^2 \left(\Im B_2 + \frac{\Im B_2'}{2} \right) \right. \\ - \sum_{n=1}^{\infty} \left(\frac{\alpha}{2}\right)^{4n} \left[\Im B_{4n} \left(\frac{G_{4n+1}^{\infty}}{4n+1} + G_{4n}^0 \right) + \frac{\Im B_{4n}'}{4n+1} G_{4n+1}^0 \right. \\ \left. \left. + \frac{\alpha^2}{4} \left(\Im B_{2(2n+1)} \left(\frac{G_{4n+3}^{\infty}}{4n+3} + G_{2(2n+1)}^0 \right) + \frac{\Im B_{2(2n+1)}'}{4n+3} G_{4n+3}^0 \right) \right] \right\} \end{array} \right)}_{F_{II}}. \tag{26}$$

Careful examination of Eqs. (23), (24), (25) and (26) reveals a qualitative similarity between Atkinson et al.'s [6] formulae and those obtained in the present analysis, considering that N_I, N_{II} and F_I, F_{II}, respectively, are double sums of terms involving the angle ϕ_o. The main difference (and main advantage) of the formulae deduced during the present study is that the contact semi-angle ω_o enters also into the calculations. This is not the case for Atkinson et al.'s solution who assumed point loading. Moreover, the present analysis provides

"closed-form" analytic expressions rather than coefficients in tabulated form. For the two solutions to become comparable to each other, a very small arbitrary value must be ascribed to the angle ω_o of the present solution to simulate as close as possible point loading.

The comparison of the two solutions is implemented in Fig. 9 where both K_{I} and K_{II} are plotted against angle ϕ_o for a disc with $R_{\mathrm{O}} = 0.05$ m, $t = 0.01$ m and $P_{\mathrm{frame}} = 20$ kN. Four α/R_{O} ratios are considered equal to 0.1, 0.2, 0.3 and 0.4. A very small contact semi-angle ω_o equal to $0.001°$ is assumed for the present solution. The number n of additional terms used (beyond the closed-form ones) for the calculations related to the present solution are equal to 1 for $\alpha/R_{\mathrm{O}} = 0.1$ and 0.2, $n = 2$ for $\alpha/R_{\mathrm{O}} = 0.3$ and $n = 3$ for $\alpha/R_{\mathrm{O}} = 0.4$ (convergence is satisfactory), while for Atkinson et al.'s solution, all five terms provided in tabular form were used.

To further assess the present analysis, comparison is made in Fig. 9 also against the results of a recently obtained solution for the SIFs, in case of a cracked circular disc under uniformly distributed pressure [5], which is valid under the assumption of very short cracks with respect to the disc's radius. Again, a very small contact semi-angle $\omega_o = 0.001°$ is considered, while for static equivalency, the uniformly distributed pressure is assumed equal to $p = P_{\mathrm{frame}}/2R_{\mathrm{O}}\omega_o t$. The respective formulae for both the mode-I and mode-II SIFs, $K_{\mathrm{I}}^{\mathrm{ShortCr}}$, $K_{\mathrm{II}}^{\mathrm{ShortCr}}$, are given in "Appendix VI". In these formulae, $t_{1,2} = R_{\mathrm{O}}e^{\mp i(\phi_o - \omega_o)}$ are the end points of the first encountered loaded arc on L_O.

As it is seen from Fig. 9a, b, for relatively short cracks ($\alpha/R_{\mathrm{O}} \leq 0.2$) all three solutions considered are almost identical all over the range of validity of these solutions (corresponding to positive K_{I}-values). The difference between the present analysis and that by Atkinson et al. [6] does not exceed 5.5 % (for $\phi_o = 0°$) and tends to zero as $\phi_o \to \phi_{o,\mathrm{cr}}$. On the contrary, the difference between the present solution and that for cracked discs with short cracks under uniform load is zero for $\phi_o = 0°$ and tends to about 4.5 % as $\phi_o \to \phi_{o,\mathrm{cr}}$. For $\alpha/R_{\mathrm{O}} > 0.2$, the differences between the three solutions start increasing. For example, for $\alpha/R_{\mathrm{O}} = 0.4$, the mode-I SIF for $\phi_o = 0°$ according to Atkinson et al.'s solution exceeds those of the present analysis by about 19 % (for higher ϕ_o values, the difference becomes smaller tending to zero as $\phi_o \to \phi_{o,\mathrm{cr}}$). On the other hand, the solution by Markides et al. [5] is identical to the present one for $\phi_o = 0°$ and the difference increases with increasing ϕ_o, finally reaching a maximum value equal to about 18 % as $\phi_o \to \phi_{o,\mathrm{cr}}$. Concerning the mode-II SIF, the conclusions, concerning the discrepancies between the three solutions, are similar to the ones related to K_{I}, both from quantitative and qualitative point of view.

The differences detected between the three solutions for relatively long cracks should be definitely expected since the role of the boundary conditions becomes more decisive compared to that for shorter cracks given that for the latter the crack tip is more or less insensitive to the exact conditions prevailing at the disc–jaw interface (length of the contact arc, distribution of pressure).

4 Discussion

In this section, some crucial aspects of the centrally cracked circular disc will be discussed, in the light of the as-above-obtained and validated solution, keeping always in mind that the specific configuration is closely related to the application of the cracked Brazilian disc for the determination of fracture toughness.

The first point that must be highlighted is that the stress field along the boundary of the elliptic hole imposes a rotation tendency on the hole which in turn imposes a rotational rigid-body-motion tendency to the disc itself. This is true for any arbitrary angle ϕ_o different from zero (or π) and $\pi/2$ (or $3\pi/2$). Under ideal conditions (perfectly frictionless pressure), it is expected that the disc would rotate so that in its final equilibrium position, the long axis of the elliptic hole would be normal to the symmetry axis of the external load. Such a rotation is not observed in praxis since frictional stresses $\sigma_{r\phi}$ are developed along the disc–jaw interface prohibiting free rigid body rotation. In other words, the rotational moment M appearing at the disc's centre due to the nature of the stress field imposed by radial pressure is balanced by the moment of the respective frictional stresses developed. A schematic representation of the problem is shown in Fig. 10a for the case with $m = 1$, i.e. for the mathematic crack of length 2α. It is seen from this figure that in order for the moment developed at the disc's centre to be balanced, a Coulomb friction $\sigma_{r\phi} = \eta P(\phi)$ (η is the respective coefficient of friction between the disc and the jaw) must be inevitably considered along the disc–jaw contact arc. In addition, taking into account the inevitable deformability of the disc–jaw pair, a second kind of friction stresses is developed due to the incompatibility of the local displacement field in the immediate vicinity of the disc–jaw contact arc. Friction stresses concern engineering community [24,25] since in some cases, they are responsible for premature disc cracking at points away from the disc's centre rendering the Brazilian-disc test's outcomes questionable. For the case of an intact disc, the friction stresses due to the displacement's incompatibility were recently quantified [26].
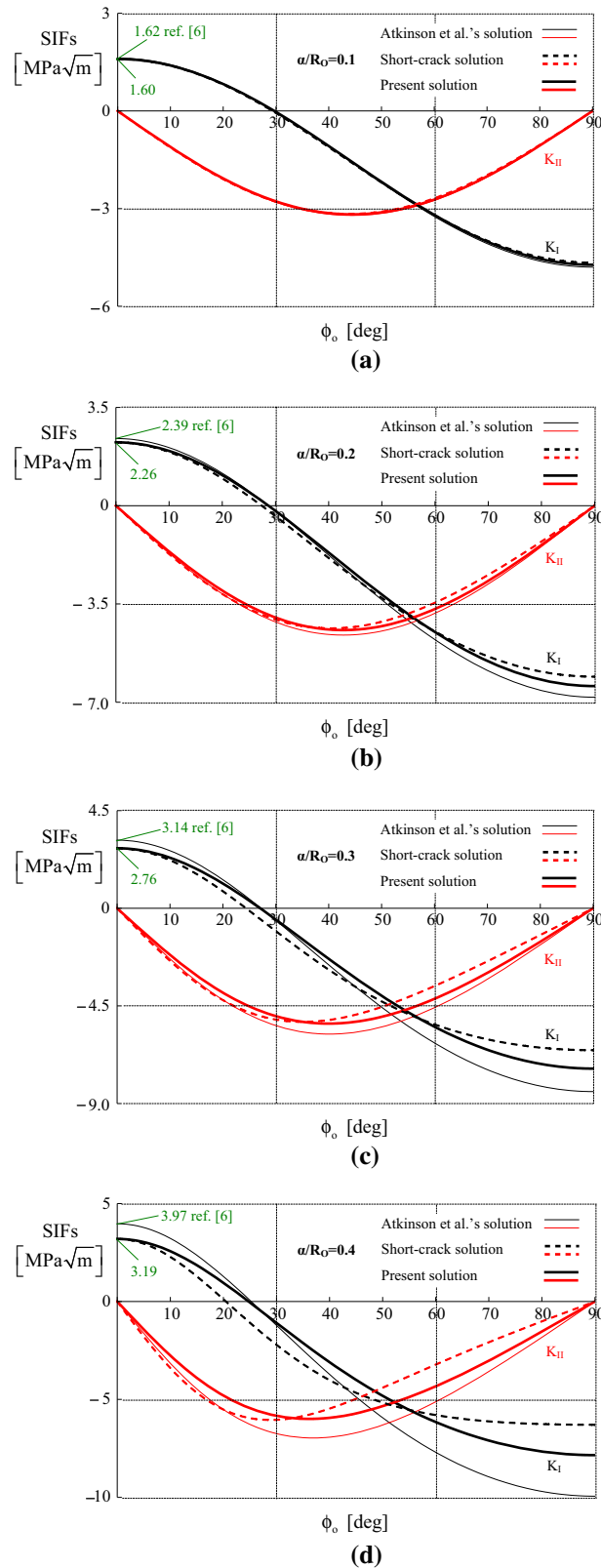
Fig. 9 The variation of the mode-I and mode-II SIFs versus the inclination of the crack axis according to the present solution, in juxtaposition to the respective one by Atkinson et al. [6] and that of Ref. [5], for $\alpha/R_O = 0.1$ (**a**), $\alpha/R_O = 0.2$ (**b**), $\alpha/R_O = 0.3$ (**c**) and $\alpha/R_O = 0.4$ (**d**)
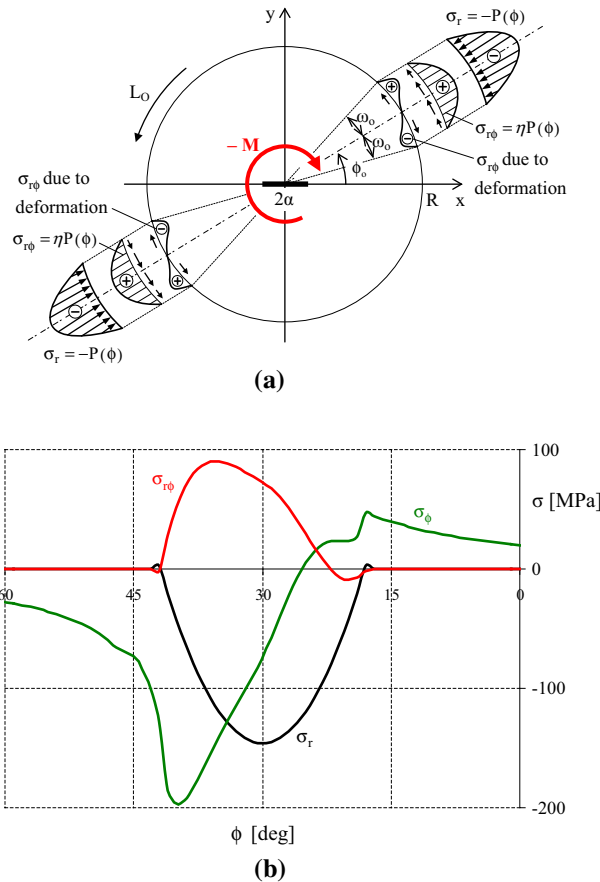
Fig. 10 **a** The rotation tendency of the cracked disc due to the overall asymmetry of the configuration and the respective friction stress distributions balancing this tendency in praxis. **b** The actual variation of the stress components along the disc's periphery in case all three stress distributions along the contact arc are taken into account

Strictly speaking, the only possibility to achieve global equilibrium of the disc (and thus to achieve the correct static solution of the problem) is to superimpose these additional loading conditions (i.e. the $\{M; \sigma_{r\phi}\}$ couple) to the problem of the disc loaded exclusively by a radial pressure distribution σ_r. Ignoring these additional loading conditions restricts the validity of the solutions obtained for the stress and displacement fields only in the immediate vicinity of the hole (crack). In case full-field solutions are to be obtained, the present solution (as well as any other of a cracked disc not taking under consideration friction stresses on the loaded arc) should be carefully reconsidered.

In this direction, an effort was recently undertaken to quantify the friction stresses required to maintain the disc's global equilibrium and also to determine the respective stress fields. For this target to be accomplished, the magnitude of the central moment M is determined directly from the forces obtained through an "inverse" second fundamental problem. Preliminary results of this effort can be seen in Fig. 10b in which the exact boundary conditions along the cracked disc's periphery (including the loaded arc) are plotted taking into account all three stress distributions (radial and the two tangential ones) depicted in Fig. 10a. In order for Fig. 10b to be drawn, a PMMA disc of radius $R_O = 0.05$ m and thickness $t = 0.01$ m with a central mathematic crack ($m = 1$) of length $2\alpha = 0.2R_O$ at an angle $\phi_o = 30°$ with respect to the symmetry axis of the pressure induced was considered. The disc is compressed under plane strain conditions between the ISRM curved steel jaws by an overall external force $P_{\text{frame}} = 20$ kN. The coefficient of friction η along the disc–jaw pair was set equal to 0.5. Both ω_o and P_c are obtained from the respective contact problem. It is very interesting to observe from Fig. 10b that both the shear- and the tangential-stress-component ($\sigma_{r\phi}$ and σ_ϕ) distributions are not symmetric with respect to the symmetry axis of the radial stress component σ_r.

Along the above line of thought, the point concerning the accuracy and convergence of the present solution at points close enough to the disc's boundary (a point discussed shortly also in Sect. 2.2) is here reconsidered.

Clearly, in case L is not very small compared to L_O, so that apart from $\varphi_o(\zeta)$ and $\psi_o(\zeta)$ some additional $\varphi_*(\zeta)$ and $\psi_*(\zeta)$ also exist on L_O, then in order for the initial global equilibrium to be maintained, extra boundary conditions counterbalancing these $\varphi_*(\zeta)$ and $\psi_*(\zeta)$ should be imposed to the loaded rim. Such boundary conditions could be connected to the friction stresses (the existence of which was justified in the previous paragraph) which were ignored in the present analysis. In such a case, $\varphi_*(\zeta)$ and $\psi_*(\zeta)$ could be deduced by taking into account the central moment M considered in previous paragraph. Nonetheless, it should be stressed that the above considerations concern the general case of asymmetric-problem configurations. In case $\phi_o = 0°$, which is related to the determination of K_{IC}, the solution remains accurate even for long elliptic holes and, for any load level, since then the stress and displacement states on the outer periphery turn up to be the same for both the elliptically perforated disc and the ring rendering the infinite-region assumption pretty legitimated.

The second crucial point that must be carefully explored is the possible contact of the crack lips. Indeed, it is well documented in the literature [6,9–11,18,20,21] that beyond a critical ϕ_o -value (depending among others on the initial distance between the crack lips) contact stresses are generated since the crack lips come in contact to each other. The specific problem is very complicated especially in case of non-mathematic cracks, as it is the elliptic hole considered here, since the contact may be partial, realized only along a finite portion of their lip's length. Therefore, an additional parameter enters in the problem, i.e. the length of the portion of the crack lips coming in contact. The solution described in Sect. 2 permits the accurate determination of the crack's deformed shape and therefore the quantification of its portion along which the crack lips are in mutual contact.

The specific feature of the present analysis is visualized in Fig. 11a–d in which the deformed shape of a disc with an elliptic hole is drawn in juxtaposition to its initial configuration. Figure 11a is drawn for a PMMA disc with $R_O = 0.05$ m, $t = 0.01$ m and a central elliptic crack of semi-length $\alpha = 0.6R_O$ and $\alpha/b = 20$ at an angle $\phi_o = 50°$. Again, the disc is compressed between the ISRM steel jaws by an overall external force $P_{frame} = 75$ kN, and ω_o, P_c are obtained from the respective contact problem. The results are obtained for plane strain conditions using $n = 3$ additional terms of the respective series expansions. It is very interesting to observe (see the magnified view Fig. 11b) both the partial contact of the crack lips and the deformed configuration of the initially elliptic hole: its axis is rotated clockwise with respect to its initial orientation, while at the same moment, its shape is distorted tending to a nonlinear sigmoid configuration. On the other hand, Fig. 11c, d is drawn for an elliptically perforated disc of the same dimensions and material as previously mentioned, but for $\alpha/b = 6$ (with $\alpha = 0.6R_O$), subjected to an overall external load $P_{frame} = 150$ kN at an angle $\phi_o = 70°$, and ω_o arbitrarily predefined, equal to $2°$. P_c is now obtained through Eq. (12). Although the specific load level is of only theoretical importance (its application is feasible due to the linear elasticity assumption), it is believed that Fig. 11c offers a very clear view of the perforated disc's deformation tendency. In addition, this theoretical example demonstrates the unique capability of the present solution to provide naturally sound results for any configuration, even for combinations of parameters leading to partial contact of the crack lips along the middle region of their length rather than close to their tips (see the magnified view in Fig. 11d).

5 Conclusions

The finite circular disc with a central elliptic hole was considered analytically. Emphasis was placed to the determination of the complex potentials characterizing the equilibrium of the disc under a parabolic distribution of radial pressure acting along two finite arcs of its periphery. Knowledge of the complex potentials permitted determination of both the stress and displacement fields all over the disc (ignoring the rotation tendency due to the asymmetric configuration).

In the second part of the study, attention was paid to the limiting case when the minor semi-axis of the elliptic hole tends to zero, and therefore, the elliptic hole tends to the mathematical crack with zero distance between its lips. Taking advantage of the complex potentials, it was possible to obtain analytic expressions for the stress intensity factors characterizing the intensity of the stress field in the vicinity of the tips of the crack.

The formulae obtained were compared against the respective ones introduced by Atkinson et al. and also against the respective ones of a recently proposed solution of a similar problem, i.e. that of a disc with a short central crack under uniform radial pressure. The comparison revealed that for short cracks (i.e. for crack length over disc radius ratios lower than 0.2), all three solutions provide almost identical results. For longer cracks, deviations between the three solutions appear approaching even 20 % in case the α/R_O ratio exceeds 0.4.

The main advantages of the present solution against previous ones can be summarized as follows:

i.   The load distribution considered, i.e. parabolically varying radial pressure, is closer to the actual pressure distribution along the disc–jaw interface as it is obtained from the solution of the respective contact
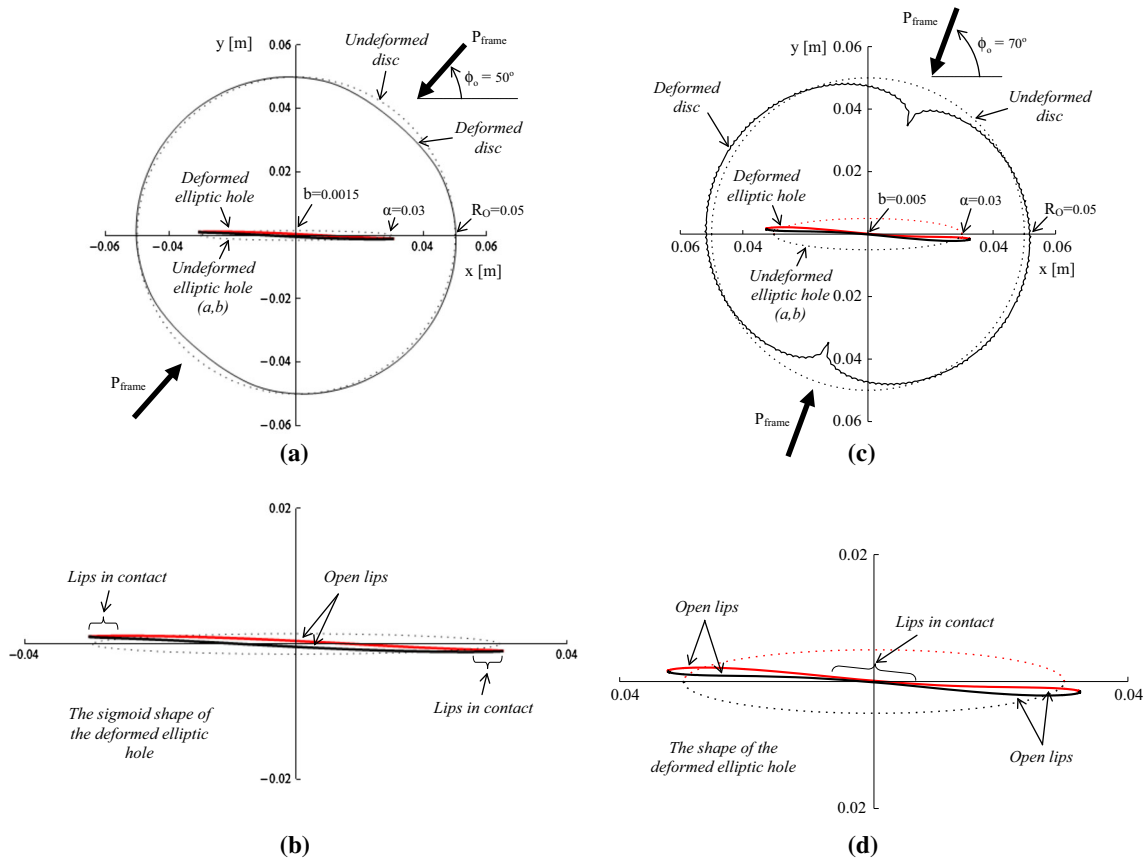
Fig. 11 a The deformed shape of the disc and the hole in case the loading imposed leads to partial contact of the hole's lips in the vicinity of the tips and **b** a magnified view of the deformed shape of the hole showing the partial closure of the lips and also the rotation and distortion of the ellipse's axis. **c** The deformed shape of the disc and the hole in case the loading imposed leads to partial contact of the hole's lips at the central portion of the crack's axis and **d** a magnified view of the deformed shape of the hole

problem [12,13]. Previous solutions considered either uniformly distributed pressure [5] or even a point load (i.e. force along a generatrix of the disc's periphery) [6].

ii. The solution is flexible because the length of the contact arc can be either considered equal to an arbitrary predefined value or it can be obtained from the solution of the respective contact problem of the intact disc–jaw problem assuming that the presence of the hole (crack) does not influence the conditions along the disc's boundary (i.e. for crack lengths not exceeding the radius of the disc).

iii. The formulae obtained for the stress and displacement fields as well as for the stress intensity factors, although relatively lengthy, are "analytic" and can be easily used (even with the aid of commercial software) since there is no need to resort to tabulated values. Moreover, using even a relatively small number of additional terms of the respective series expansions, the accuracy obtained is very satisfactory, at least for points not very close to the disc's boundary.

iv. The solution for the displacement field of the elliptic hole's boundary permits determination of the deformed shape of the initially elliptic hole and, in addition, it permits the determination of the portions of the hole's lips that came in contact against each other and therefore along which contact stresses are generated.

v. An alternative definition for the stress intensity factors through $\Phi(z)$ is introduced in the case of an elliptic crack.

The main conclusions drawn can be summarized as follows:

i The tensile normal stress at the tip of the elliptic hole ($x = \alpha$) for b/α ratios exceeding 0.2 is not sensitive to the exact b/α value. Especially, for $\phi_o = 0°$ and $0.2 < b/\alpha \leq 0.5$, σ_y tends to P_c. For lower b/α ratios, σ_y at $x = \alpha$ increases very rapidly and the linear elasticity assumption collapses.

ii The range of ϕ_o values, for which the present solution for the SIFs (and any other similar one) is valid, is terminated when K_I becomes negative due to the fact that from this point on, the crack lips come in mutual contact, and contact stresses appear (both normal and shear) altering the boundary conditions. The angle ϕ_{cr} at which K_I changes sign depends on both the extent of the contact arc $2\omega_o$ and also on the length 2α of the crack.

iii The values of the SIFs depend on the length of the contact arc. It is a fortunate fact, however, that for moderate ω_o-values (not exceeding $12.5°$), this dependence is very small and can be ignored. Therefore, in practical applications, in which brittle materials are tested using the cracked Brazilian-disc test, it is absolutely safe to assume that the simplified expressions for the SIFs (based on the assumption of an arbitrarily determined small contact angle) are valid, and the error due to the deformability of the disc–jaw elastic system is ignorable.

iv In general, the dependence of K_I on the disc's thickness is non-monotonous, and a clear maximum of the $K_I - K_I(t)$ graph is observed. For discs of diameter equal to about $100\,mm$, the plane strain assumption appears to be valid for disc's thickness exceeding $10\,mm$. There is no need therefore to test thicker specimens in case the fracture toughness of brittle materials is to be determined using the cracked Brazilian-disc test.

Before concluding, it should be emphasized once again that the solution described was obtained under a number of simplifying assumptions. The most restricting one is perhaps that the ring's boundary is insensitive to the presence of the crack; therefore, the superposition principle was used in order to obtain the complex potentials as the sum of those characterizing the equilibrium of a finite ring and those characterizing the elliptic hole in an infinite plate. This is in fact the technique accepted also by Muskhelishvili [8] in the case of an infinite long strip with a circular hole. Although any assumption is finally subjected to the litmus test of being validated against either experimental reality or previous widely accepted analytic solutions (the latter is the test successfully passed by the present solution), it is to be accepted that in case of crack lengths exceeding the disc's radius, and for the general case $\phi_o \neq 0°$ and $\phi_o \neq 90°$, the present solution (as well as any other previously introduced) is to be considered with caution and reservation.

One might think at this point that the solution for the elliptically perforated disc could be obtained based on the respective one of the intact disc instead of that for a ring-shaped body (as it was done in the present analysis). This statement sounds meaningful; however, the fact that the ring's solution has been obtained in series form makes it more convenient than that of the intact disc. Indeed, the ring's solution, though very lengthy, is at least relieved from the presence of extra distinct poles (appearing in the intact disc's solution at the end points of the loaded arcs) apart from those at infinity and at the zero point, increasing the difficulty of the procedure.

The second restricting assumption is that the disc is loaded by exclusively a distribution of radial pressure. In other words, the influence of any kind of friction along the contact arc (tangential stresses) was ignored. Although it is the privilege of the researcher to define the mathematic problem he intends to solve (considering that all assumptions are clearly and unambiguously stated), it is to be accepted that the specific assumption limits the practical applicability of the present solution. This is because in case the test is implemented using the device suggested by ISRM for the standardized Brazilian-disc test [1,15], it is definitely proven [24–26] that complex friction stress distributions are developed, the magnitude of which is not ignorable. Moreover, neglecting friction imposes an additional complication since the static equilibrium of the disc becomes questionable: the inherent lack of symmetry of the configuration studied (unless the long semi-axis of the elliptic hole is parallel or normal to the axis of symmetry of the load imposed) tends to cause a rigid body rotation rendering the assumption of static equilibrium under radial pressure only erroneous.

In spite of the above limitations, it is believed that the present study offers a valuable tool, not only theoretical but also of practical value, to researchers working with the cracked Brazilian disc configuration: the conclusions drawn could be the chargeable spark in the direction of modifying the relative standards for the determination of K_{IC}, while, on the other hand, they could be used in the direction of assessing and validating sophisticated numerical models which nowadays are widely used for the parametric study of a series of practical aspects of the specific configuration.

Appendix I: The coefficients of the series expansions of Eqs. (1) and (2)

$$b_0 = \left(\frac{2\omega_o - \sin 2\omega_o}{4 \sin^2 \omega_o} - \omega_o \right) \frac{R_O^2}{R_O^2 - R_I^2}$$

$$B_2 = \left(\frac{\omega_o - \sin 2\omega_o}{2 \sin^2 \omega_o} + \frac{\sin 2\omega_o \cos 2\omega_o}{4 \sin^2 \omega_o} + \sin 2\omega_o \right) \frac{3\left(R_O^2 - R_I^2\right) - R_O^4\left(R_O^{-2} - R_I^{-2}\right)}{3\left(R_O^2 - R_I^2\right)^2 + \left(R_O^6 - R_I^6\right)\left(R_O^{-2} - R_I^{-2}\right)}$$
$$\cdot (\cos 2\phi_o - i \sin 2\phi_o)$$

$$B_{-2} = \left(\frac{\omega_o - \sin 2\omega_o}{2 \sin^2 \omega_o} + \frac{\sin 2\omega_o \cos 2\omega_o}{4 \sin^2 \omega_o} + \sin 2\omega_o \right) \frac{R_O^4\left(R_I^2 - R_O^2\right) + \left(R_I^6 - R_O^6\right)}{3\left(R_O^2 - R_I^2\right)^2 + \left(R_O^6 - R_I^6\right)\left(R_O^{-2} - R_I^{-2}\right)}$$
$$\cdot (\cos 2\phi_o + i \sin 2\phi_o)$$

$$B_{4n} = \left(\frac{\sin 4n\omega_o}{4n \sin^2 \omega_o} + \frac{\sin 2\omega_o \cos 4n\omega_o - 2n \cos 2\omega_o \sin 4n\omega_o}{2\left(4n^2 - 1\right) \sin^2 \omega_o} - \frac{\sin 4n\omega_o}{2n} \right)$$
$$\cdot \frac{(1 + 4n)\left(R_O^2 - R_I^2\right) R_O^{-2(2n-1)} - \left[R_O^{-2(4n-1)} - R_I^{-2(4n-1)}\right] R_O^{2(2n+1)}}{\left(1 - 16n^2\right)\left(R_O^2 - R_I^2\right)^2 - \left[R_O^{2(4n+1)} - R_I^{2(4n+1)}\right]\left[R_O^{-2(4n-1)} - R_I^{-2(4n-1)}\right]} (\cos 4n\phi_o - i \sin 4n\phi_o)$$

$$B_{-4n} = \left(\frac{\sin 4n\omega_o}{4n \sin^2 \omega_o} + \frac{\sin 2\omega_o \cos 4n\omega_o - 2n \cos 2\omega_o \sin 4n\omega_o}{2\left(4n^2 - 1\right) \sin^2 \omega_o} - \frac{\sin 4n\omega_o}{2n} \right)$$
$$\cdot \frac{(1 - 4n)\left(R_O^2 - R_I^2\right) R_O^{2(2n+1)} - \left[R_O^{2(4n+1)} - R_I^{2(4n+1)}\right] R_O^{-2(2n-1)}}{\left(1 - 16n^2\right)\left(R_O^2 - R_I^2\right)^2 - \left[R_O^{2(4n+1)} - R_I^{2(4n+1)}\right]\left[R_O^{-2(4n-1)} - R_I^{-2(4n-1)}\right]} (\cos 4n\phi_o + i \sin 4n\phi_o)$$

$$B_{2(2n+1)} = \left[\frac{\sin 2(2n+1)\omega_o}{2(2n+1) \sin^2 \omega_o} + \frac{\sin 2\omega_o \cos 2(2n+1)\omega_o - (2n+1) \cos 2\omega_o \sin 2(2n+1)\omega_o}{8n(n+1) \sin^2 \omega_o} \right.$$
$$\left. - \frac{\sin 2(2n+1)\omega_o}{2n+1} \right] \frac{(4n+3)\left(R_O^2 - R_I^2\right) R_O^{-4n} - \left[R_O^{-2(4n+1)} - R_I^{-2(4n+1)}\right] R_O^{4(n+1)}}{\left[1 - 4(2n+1)^2\right]\left(R_O^2 - R_I^2\right)^2 - \left[R_O^{2(4n+3)} - R_I^{2(4n+3)}\right]\left[R_O^{-2(4n+1)} - R_I^{-2(4n+1)}\right]}$$
$$\cdot [\cos 2(2n+1)\phi_o - i \sin 2(2n+1)\phi_o]$$

$$B_{-2(2n+1)} = \left[\frac{\sin 2(2n+1)\omega_o}{2(2n+1) \sin^2 \omega_o} + \frac{\sin 2\omega_o \cos 2(2n+1)\omega_o - (2n+1) \cos 2\omega_o \sin 2(2n+1)\omega_o}{8n(n+1) \sin^2 \omega_o} \right.$$
$$\left. - \frac{\sin 2(2n+1)\omega_o}{2n+1} \right] \frac{(4n+1)\left(R_I^2 - R_O^2\right) R_O^{4(n+1)} + \left[R_I^{2(4n+3)} - R_O^{2(4n+3)}\right] R_O^{-4n}}{\left[1 - 4(2n+1)^2\right]\left(R_O^2 - R_I^2\right)^2 - \left[R_O^{2(4n+3)} - R_I^{2(4n+3)}\right]\left[R_O^{-2(4n+1)} - R_I^{-2(4n+1)}\right]}$$
$$\cdot [\cos 2(2n+1)\phi_o + i \sin 2(2n+1)\phi_o]$$

$$B_0' = \left(\frac{\omega_o - \sin 2\omega_o}{\sin^2 \omega_o} + \frac{\sin 2\omega_o \cos 2\omega_o}{2 \sin^2 \omega_o} + 2 \sin 2\omega_o \right) \frac{R_I^2\left(2R_I^2 - R_O^2 - R_O^6 R_I^{-4}\right)}{3\left(R_O^2 - R_I^2\right)^2 + \left(R_O^6 - R_I^6\right)\left(R_O^{-2} - R_I^{-2}\right)}$$
$$\cdot (\cos 2\phi_o - i \sin 2\phi_o)$$

$$B_2' = \left(\frac{\sin 4\omega_o}{\sin^2 \omega_o} + 2\frac{\sin 2\omega_o \cos 4\omega_o - 2 \cos 2\omega_o \sin 4\omega_o}{3 \sin^2 \omega_o} - 2 \sin 4\omega_o \right)$$
$$\cdot \frac{R_I^2\left(3 - 4R_O^{-2}R_I^2 + R_O^8 R_I^{-8}\right)}{15\left(R_O^2 - R_I^2\right)^2 + \left(R_O^{10} - R_I^{10}\right)\left(R_O^{-6} - R_I^{-6}\right)} (\cos 4\phi_o - i \sin 4\phi_o)$$

$$b_{-2}' = \left(\frac{2\omega_o - \sin 2\omega_o}{2 \sin^2 \omega_o} - 2\omega_o \right) \frac{R_O^2 R_I^2}{R_O^2 - R_I^2}$$

$$B_{-4}' = \left(\frac{\omega_o - \sin 2\omega_o}{\sin^2 \omega_o} + \frac{\sin 2\omega_o \cos 2\omega_o}{2 \sin^2 \omega_o} + 2 \sin 2\omega_o \right) \frac{R_O^2 R_I^2\left(R_I^4 + 2R_O^2 R_I^2 - 3R_O^4\right)}{3\left(R_O^2 - R_I^2\right)^2 + \left(R_O^6 - R_I^6\right)\left(R_O^{-2} - R_I^{-2}\right)}$$

$$\cdot \left(\cos 2\phi_o + i \sin 2\phi_o \right)$$

$$B'_{4n} = \left[\frac{\sin 2(2n+1)\omega_o}{2(2n+1)\sin^2 \omega_o} + \frac{\sin 2\omega_o \cos 2(2n+1)\omega_o - (2n+1)\cos 2\omega_o \sin 2(2n+1)\omega_o}{8n(n+1)\sin^2 \omega_o} \right.$$

$$\left. - \frac{\sin 2(2n+1)\omega_o}{2n+1} \right] \left\{ (4n+1)R_I^2 \left[(4n+3)\left(R_I^2 - R_O^2 \right) R_O^{-4n} - \left[R_I^{-2(4n+1)} - R_O^{-2(4n+1)} \right] R_O^{4(n+1)} \right] \right.$$

$$\left. + R_I^{-2(4n+1)} \left[(4n+1)\left(R_I^2 - R_O^2 \right) R_O^{4(n+1)} + \left[R_I^{2(4n+3)} - R_O^{2(4n+3)} \right] R_O^{-4n} \right] \right\}$$

$$\Big/ \left\{ \left[1 - 4(2n+1)^2 \right] \left(R_O^2 - R_I^2 \right)^2 - \left[R_O^{2(4n+3)} - R_I^{2(4n+3)} \right] \left[R_O^{-2(4n+1)} - R_I^{-2(4n+1)} \right] \right\}$$

$$\cdot \left[\cos 2(2n+1)\phi_o - i \sin 2(2n+1)\phi_o \right]$$

$$B'_{2(2n+1)} = \left[\frac{\sin 4(n+1)\omega_o}{4(n+1)\sin^2 \omega_o} + \frac{\sin 2\omega_o \cos 4(n+1)\omega_o - 2(n+1)\cos 2\omega_o \sin 4(n+1)\omega_o}{2\left[4(n+1)^2 - 1 \right] \sin^2 \omega_o} \right.$$

$$\left. - \frac{\sin 4(n+1)\omega_o}{2(n+1)} \right] \left\{ (4n+3)R_I^2 \left[(4n+5)\left(R_I^2 - R_O^2 \right) R_O^{-2(2n+1)} - \left[R_I^{-2(4n+3)} - R_O^{-2(4n+3)} \right] R_O^{2(2n+3)} \right] \right.$$

$$\left. + R_I^{-2(4n+3)} \left[(4n+3)\left(R_I^2 - R_O^2 \right) R_O^{2(2n+3)} + \left[R_I^{2(4n+5)} - R_O^{2(4n+5)} \right] R_O^{-2(2n+1)} \right] \right\}$$

$$\Big/ \left\{ \left[1 - 16(n+1)^2 \right] \left(R_O^2 - R_I^2 \right)^2 - \left[R_O^{2(4n+5)} - R_I^{2(4n+5)} \right] \left[R_O^{-2(4n+3)} - R_I^{-2(4n+3)} \right] \right\}$$

$$\cdot \left[\cos 4(n+1)\phi_o - i \sin 4(n+1)\phi_o \right]$$

$$B'_{-4(n+1)} = \left[\frac{\sin 2(2n+1)\omega_o}{2(2n+1)\sin^2 \omega_o} + \frac{\sin 2\omega_o \cos 2(2n+1)\omega_o - (2n+1)\cos 2\omega_o \sin 2(2n+1)\omega_o}{8n(n+1)\sin^2 \omega_o} \right.$$

$$\left. - \frac{\sin 2(2n+1)\omega_o}{2n+1} \right] \left\{ (4n+3)R_I^2 \left[(4n+1)\left(R_I^2 - R_O^2 \right) R_O^{4(n+1)} + \left[R_I^{2(4n+3)} - R_O^{2(4n+3)} \right] R_O^{-4n} \right] \right.$$

$$\left. - R_I^{2(4n+3)} \left[(4n+3)\left(R_I^2 - R_O^2 \right) R_O^{-4n} - \left[R_I^{-2(4n+1)} - R_O^{-2(4n+1)} \right] R_O^{4(n+1)} \right] \right\}$$

$$\Big/ \left\{ \left[1 - 4(2n+1)^2 \right] \left(R_O^2 - R_I^2 \right)^2 - \left[R_O^{2(4n+3)} - R_I^{2(4n+3)} \right] \left[R_O^{-2(4n+1)} - R_I^{-2(4n+1)} \right] \right\}$$

$$\cdot \left[\cos 2(2n+1)\phi_o + i \sin 2(2n+1)\phi_o \right]$$

$$B'_{-2(2n+1)} = \left[\frac{\sin 4n\omega_o}{4n \sin^2 \omega_o} + \frac{\sin 2\omega_o \cos 4n\omega_o - 2n \cos 2\omega_o \sin 4n\omega_o}{2\left(4n^2 - 1 \right) \sin^2 \omega_o} - \frac{\sin 4n\omega_o}{2n} \right]$$

$$\cdot \left\{ (1+4n)R_I^2 \left[(1-4n)\left(R_O^2 - R_I^2 \right) R_O^{2(2n+1)} - \left[R_O^{2(4n+1)} - R_I^{2(4n+1)} \right] R_O^{-2(2n-1)} \right] \right.$$

$$\left. + R_I^{2(4n+1)} \left[(1+4n)\left(R_O^2 - R_I^2 \right) R_O^{-2(2n-1)} - \left[R_O^{-2(4n-1)} - R_I^{-2(4n-1)} \right] R_O^{2(2n+1)} \right] \right\}$$

$$\Big/ \left\{ \left(1 - 16n^2 \right) \left(R_O^2 - R_I^2 \right)^2 - \left[R_O^{2(4n+1)} - R_I^{2(4n+1)} \right] \left[R_O^{-2(4n-1)} - R_I^{-2(4n-1)} \right] \right\}$$

$$\cdot \left(\cos 4n\phi_o + i \sin 4n\phi_o \right)$$

Appendix II: The principal parts, i.e. parts of the following functions in brackets that spawn poles at the point at infinity and at $\zeta = 0$, entering in Eqs. (9) and (10)

$$G^\infty_{4n+1}(\zeta) := \underset{\zeta=\infty}{P.P.} \left(\zeta + \frac{m}{\zeta} \right)^{4n+1} = \sum_{k=0}^{2n} \frac{(4n+1)!}{k!(4n+1-k)!} m^k \zeta^{2(2n-k)+1}$$

$$G^\infty_{4n+3}(\zeta) := \underset{\zeta=\infty}{P.P.} \left(\zeta + \frac{m}{\zeta} \right)^{4n+3} = \sum_{k=0}^{2n+1} \frac{(4n+3)!}{k!(4n+3-k)!} m^k \zeta^{2(2n-k)+3}$$

$$G^0_{4n}(\zeta) := \underset{\zeta=0}{P.P.} \left(\frac{1}{\zeta} + m\zeta \right)^{4n} = \sum_{k=0}^{2n-1} \frac{(4n)!}{k!(4n-k)!} m^k \zeta^{2(k-2n)+1} + \sum_{k=0}^{2n} \frac{(4n)!}{k!(4n-k)!} m^{k+1} \zeta^{2(k-2n)-1}$$

$$G^0_{2(2n+1)}(\zeta) := \underset{\zeta=0}{P.P.} \left(\frac{1}{\zeta} + m\zeta \right)^{2(2n+1)}$$

$$= \sum_{k=0}^{2n} \frac{[2(2n+1)]!}{k!\,[2(2n+1)-k]!} m^k \zeta^{2(k-2n)-1} + \sum_{k=0}^{2n+1} \frac{[2(2n+1)]!}{k!\,[2(2n+1)-k]!} m^{k+1} \zeta^{2(k-2n)-3}$$

$$G^0_{4n+1}(\zeta) := \underset{\zeta=0}{P.P.} \left(\frac{1}{\zeta} + m\zeta \right)^{4n+1} = \sum_{k=0}^{2n} \frac{(4n+1)!}{k!(4n+1-k)!} m^k \zeta^{2(k-2n)-1}$$

$$G^0_{4n+3}(\zeta) := \underset{\zeta=0}{P.P.} \left(\frac{1}{\zeta} + m\zeta \right)^{4n+3} = \sum_{k=0}^{2n+1} \frac{(4n+3)!}{k!\,(4n+3-k)!} m^k \zeta^{2(k-2n)-3}$$

$$G^\infty_{4n}(\zeta) := \underset{\zeta=\infty}{P.P.} \left(\zeta + \frac{m}{\zeta} \right)^{4n} = \sum_{k=0}^{2n-1} \frac{(4n)!}{k!(4n-k)!} m^k \zeta^{2(2n-k)-1} + \sum_{k=0}^{2n} \frac{(4n)!}{k!(4n-k)!} m^{k+1} \zeta^{2(2n-k)+1}$$

$$G^\infty_{2(2n+1)}(\zeta) := \underset{\zeta=\infty}{P.P.} \left(\zeta + \frac{m}{\zeta} \right)^{2(2n+1)}$$

$$= \sum_{k=0}^{2n} \frac{[2(2n+1)]!}{k!\,[2(2n+1)-k]!} m^k \zeta^{2(2n-k)+1} + \sum_{k=0}^{2n+1} \frac{[2(2n+1)]!}{k!\,[2(2n+1)-k]!} m^{k+1} \zeta^{2(2n-k)+3}$$

Appendix III: The real, $\Re$, and imaginary, $\Im$, parts of the first six functions of Appendix II, appearing in Eqs. (14) and (15)

$$\left.\begin{array}{c} \Re G^\infty_{4n+1}(\theta) \\ \Im G^\infty_{4n+1}(\theta) \end{array}\right\} = \sum_{k=0}^{2n} \frac{(4n+1)!}{k!(4n+1-k)!} m^k \left\{ \begin{array}{c} \cos\left[2(2n-k)+1\right]\theta \\ \sin\left[2(2n-k)+1\right]\theta \end{array} \right.$$

$$\left.\begin{array}{c} \Re G^0_{4n}(\zeta) \\ \Im G^0_{4n}(\zeta) \end{array}\right\} = \sum_{k=0}^{2n-1} \frac{(4n)!}{k!(4n-k)!} m^k \left\{ \begin{array}{c} \cos\left[2(k-2n)+1\right]\theta \\ \sin\left[2(k-2n)+1\right]\theta \end{array} \right.$$

$$+ \sum_{k=0}^{2n} \frac{(4n)!}{k!(4n-k)!} m^{k+1} \left\{ \begin{array}{c} \cos\left[2(k-2n)-1\right]\theta \\ \sin\left[2(k-2n)-1\right]\theta \end{array} \right.$$

$$\left.\begin{array}{c} \Re G^0_{4n+1}(\theta) \\ \Im G^0_{4n+1}(\theta) \end{array}\right\} = \sum_{k=0}^{2n} \frac{(4n+1)!}{k!(4n+1-k)!} m^k \left\{ \begin{array}{c} \cos\left[2(k-2n)-1\right]\theta \\ \sin\left[2(k-2n)-1\right]\theta \end{array} \right.$$

$$\left.\begin{array}{c} \Re G^\infty_{4n+3}(\theta) \\ \Im G^\infty_{4n+3}(\theta) \end{array}\right\} = \sum_{k=0}^{2n+1} \frac{(4n+3)!}{k!\,(4n+3-k)!} m^k \left\{ \begin{array}{c} \cos\left[2(2n-k)+3\right]\theta \\ \sin\left[2(2n-k)+3\right]\theta \end{array} \right.$$

$$\left.\begin{array}{c} \Re G^0_{2(2n+1)}(\theta) \\ \Im G^0_{2(2n+1)}(\theta) \end{array}\right\} = \sum_{k=0}^{2n} \frac{[2(2n+1)]!}{k!\,[2(2n+1)-k]!} m^k \left\{ \begin{array}{c} \cos\left[2(k-2n)-1\right]\theta \\ \sin\left[2(k-2n)-1\right]\theta \end{array} \right.$$

$$+ \sum_{k=0}^{2n+1} \frac{[2(2n+1)]!}{k!\,[2(2n+1)-k]!} m^{k+1} \left\{ \begin{array}{c} \cos\left[2(k-2n)-3\right]\theta \\ \sin\left[2(k-2n)-3\right]\theta \end{array} \right.$$

$$\left.\begin{array}{c} \Re G^0_{4n+3}(\theta) \\ \Im G^0_{4n+3}(\theta) \end{array}\right\} = \sum_{k=0}^{2n+1} \frac{(4n+3)!}{k!\,(4n+3-k)!} m^k \left\{ \begin{array}{c} \cos\left[2(k-2n)-3\right]\theta \\ \sin\left[2(k-2n)-3\right]\theta \end{array} \right.$$

Appendix IV: The coefficients of the series expansions of Eq. (19), following from the values of the respective coefficients of Appendix I for $R_I = 0$

$$b_0 = \frac{2\omega_o - \sin 2\omega_o}{4\sin^2\omega_o} - \omega_o$$

$$B_2 = \left(\frac{\omega_o - \sin 2\omega_o}{2\sin^2\omega_o} + \frac{\sin 2\omega_o \cos 2\omega_o}{4\sin^2\omega_o} + \sin 2\omega_o\right)\frac{\cos 2\phi_o - i\sin 2\phi_o}{-R_O^2}$$

$$B'_o = \left(\frac{\omega_o - \sin 2\omega_o}{\sin^2\omega_o} + \frac{\sin 2\omega_o \cos 2\omega_o}{2\sin^2\omega_o} + 2\sin 2\omega_o\right)(\cos 2\phi_o - i\sin 2\phi_o)$$

$$B'_2 = \left(\frac{\sin 4\omega_o}{\sin^2\omega_o} + 2\frac{\sin 2\omega_o \cos 4\omega_o - 2\cos 2\omega_o \sin 4\omega_o}{3\sin^2\omega_o} - 2\sin 4\omega_o\right)\frac{\cos 4\phi_o - i\sin 4\phi_o}{-R_O^2}$$

$$B_{4n} = \left(\frac{\sin 4n\omega_o}{4n\sin^2\omega_o} + \frac{\sin 2\omega_o \cos 4n\omega_o - 2n\cos 2\omega_o \sin 4n\omega_o}{2\left(4n^2-1\right)\sin^2\omega_o} - \frac{\sin 4n\omega_o}{2n}\right)\frac{\cos 4n\phi_o - i\sin 4n\phi_o}{R_O^{4n}}$$

$$B_{2(2n+1)} = \left[\frac{\sin 2(2n+1)\omega_o}{2(2n+1)\sin^2\omega_o} + \frac{\sin 2\omega_o \cos 2(2n+1)\omega_o - (2n+1)\cos 2\omega_o \sin 2(2n+1)\omega_o}{8n(n+1)\sin^2\omega_o}\right.$$
$$\left. - \frac{\sin 2(2n+1)\omega_o}{2n+1}\right]\frac{\cos 2(2n+1)\phi_o - i\sin 2(2n+1)\phi_o}{R_O^{2(2n+1)}}$$

$$B'_{4n} = \left[\frac{\sin 2(2n+1)\omega_o}{(2n+1)\sin^2\omega_o} + \frac{\sin 2\omega_o \cos 2(2n+1)\omega_o - (2n+1)\cos 2\omega_o \sin 2(2n+1)\omega_o}{4n(n+1)\sin^2\omega_o}\right.$$
$$\left. - \frac{2\sin 2(2n+1)\omega_o}{2n+1}\right]\frac{(2n+1)\left[\cos 2(2n+1)\phi_o - i\sin 2(2n+1)\phi_o\right]}{-R_O^{4n}}$$

$$B'_{2(2n+1)} = \left\{\frac{\sin 4(n+1)\omega_o}{(n+1)\sin^2\omega_o} + 2\frac{\sin 2\omega_o \cos 4(n+1)\omega_o - 2(n+1)\cos 2\omega_o \sin 4(n+1)\omega_o}{\left[4(n+1)^2-1\right]\sin^2\omega_o}\right.$$
$$\left. - \frac{2\sin 4(n+1)\omega_o}{n+1}\right\}\frac{(n+1)\left[\cos 4(n+1)\phi_o - i\sin 4(n+1)\phi_o\right]}{-R_O^{2(2n+1)}}$$

Appendix V: Functions appearing in Eqs. (21) and (22) that indicate the first-order derivatives of the first six functions of Appendix II with respect to ζ, for $\zeta = 1$ (or after reverting to the variable z, for $z = \alpha$) and $m = 1$

$$G^\infty_{4n+1} = \sum_{k=0}^{2n}\frac{(4n+1)!}{k!(4n+1-k)!}\left[2(2n-k)+1\right]$$

$$G^0_{4n} = \sum_{k=0}^{2n-1}\frac{(4n)!}{k!(4n-k)!}\left[2(k-2n)+1\right] + \sum_{k=0}^{2n}\frac{(4n)!}{k!(4n-k)!}\left[2(k-2n)-1\right]$$

$$G^0_{4n+1} = \sum_{k=0}^{2n}\frac{(4n+1)!}{k!(4n+1-k)!}\left[2(k-2n)-1\right]$$

$$G^\infty_{4n+3} = \sum_{k=0}^{2n+1}\frac{(4n+3)!}{k!\,(4n+3-k)!}\left[2(2n-k)+3\right]$$

$$G^0_{2(2n+1)} = \sum_{k=0}^{2n}\frac{[2(2n+1)]!}{k!\,[2(2n+1)-k]!}\left[2(k-2n)-1\right] + \sum_{k=0}^{2n+1}\frac{[2(2n+1)]!}{k!\,[2(2n+1)-k]!}\left[2(k-2n)-3\right]$$

$$G^0_{4n+3} = \sum_{k=0}^{2n+1}\frac{(4n+3)!}{k!\,(4n+3-k)!}\left[2(k-2n)-3\right]$$

Appendix VI: The SIFs for a circular disc with a short central crack under uniform radial pressure [5]

$$
\begin{aligned}
K_{\mathrm{I}}^{\text{Short Cr}} = {} & \frac{P_{\text{frame}}}{2R_O\omega_o t}\sqrt{\frac{\alpha}{\pi}}\cdot\Big\{\arg\left(t_1^2-\alpha^2\right)-\arg\left(t_2^2-\alpha^2\right)+2\omega_o \\
& + \frac{2R_O^2\left(R_O^2-\alpha^2\right)\left[\left(R_O^4+\alpha^4\right)\sin 2\omega_o\cos 2\phi_o - R_O^2\alpha^2\sin 4\omega_o\right]}{R_O^8+\alpha^8-4R_O^2\alpha^2\left(R_O^4+\alpha^4\right)\cos 2\omega_o\cos 2\phi_o+2R_O^4\alpha^4\left(\cos 4\phi_o+2\cos^2 2\omega_o\right)}\Big\}
\end{aligned}
$$

$$
\begin{aligned}
K_{\mathrm{II}}^{\text{Short Cr}} = {} & \frac{P_{\text{frame}}}{2R_O\omega_o t}\sqrt{\frac{\alpha}{\pi}} \\
& \cdot\frac{-2R_O^2\left(R_O^2-\alpha^2\right)\left(R_O^4-\alpha^4\right)\sin 2\omega_o\sin 2\phi_o}{R_O^8+\alpha^8-4R_O^2\alpha^2\left(R_O^4+\alpha^4\right)\cos 2\omega_o\cos 2\phi_o+2R_O^4\alpha^4\left(\cos 4\phi_o+2\cos^2 2\omega_o\right)}
\end{aligned}
$$

References

1. ISRM (Coordinator Fowell, R.J.): Suggested methods for determining mode-I fracture toughness using CCNBD specimens. Int. J. Rock Mech. Min. **32**(1), 57–64 (1995)
2. Wang, Q.Z., Fan, H., Gou, X.P., Zhang, S.: Recalibration and clarification of the formula applied to the ISRM-suggested CCNBD specimens for testing rock fracture toughness. Rock Mech. Rock Eng. **46**, 303–313 (2013)
3. Kourkoulis, S.K., Markides, Ch.F.: Fracture toughness determined by the centrally cracked Brazilian disc test: Some critical issues in the light of an alternative analytic solution. ASTM Mater. Perform. Charact. **3**(3), 45–86 (2014)
4. Dong, S.: Theoretical analysis of the effects of relative crack length and loading angle on the experimental results for the cracked Brazilian disk testing. Eng. Fract. Mech. **75**, 2575–2581 (2008)
5. Markides, Ch.F., Pazis, D.N., Kourkoulis, S.K.: Stress intensity factors for the Brazilian disc with a short central crack: opening versus closing cracks. Appl. Math. Model. **35**(12), 5636–5651 (2011)
6. Atkinson, C., Smelser, R.E., Sanchez, J.: Combined mode fracture via the cracked Brazilian disk test. Int. J. Fract. **18**, 279–291 (1982)
7. Kolosov G.V.: Application of the Complex Variable to the Theory of Elasticity (in Russian). ONT1, Moscow-Leningrad (1935)
8. Muskhelishvili, N.I.: Some Basic Problems of the Mathematical Theory of Elasticity. Noordhoff, Groningen (1963)
9. Burniston, E.E.: An example of a partially closed Griffith crack. Int. J. Rock. Mech. Min. Sci. **5**, 17–24 (1969)
10. Tweed, J.: The determination of the stress intensity factor of a partially closed Griffith crack. Int. J. Eng. Sci. **8**(9), 793–803 (1970)
11. Thresher, R.W., Smith, F.W.: The partially closed Griffith crack. Int. J. Fract. **9**, 33–41 (1973)
12. Timoshenko, S.P., Goodier, J.N.: Theory of Elasticity. McGraw-Hill, New York (1970)
13. Kourkoulis, S.K., Markides, Ch.F., Chatzistergos, P.E.: The standardized Brazilian disc test as a contact problem. Int. J. Rock. Mech. Min. Sci. **57**, 132–141 (2012)
14. Markides, Ch.F., Kourkoulis, S.K.: The stress field in a standardized Brazilian disc: the influence of the loading type acting on the actual contact length. Rock Mech. Rock Eng. **45**(2), 145–158 (2012)
15. ISRM (Co-ordinator: Ouchterlony, F.) Suggested methods for determining the fracture toughness of rock. Int. J. Rock. Mech. Min. Sci. Geomech. Abstr. **25**, 71–96 (1988)
16. Kourkoulis, S.K., Markides, Ch.F., Pasiou, E.D.: A combined analytic and experimental study of the displacement field in a circular ring. Meccanica. **50**, 493–515 (2015)
17. Kanninen, M.F., Popelar, C.H.: Advanced Fracture Mechanics. Oxford University Press, New York (1985)
18. Pazis, D.N., Theocaris, P.S., Konstantellos, B.D.: Elastic overlapping of the crack flanks under mixed-mode loading. Int. J. Fract. **37**, 303–319 (1988)
19. Theocaris, P.S., Sakellariou, M.: A correction model for the incompatible deformations of the shear internal crack. Eng. Fract. Mech. **38**, 231–240 (1991)
20. Markides, Ch.F., Pazis, D.N., Kourkoulis, S.K.: The centrally cracked Brazilian disc: closed solutions for stresses and displacements for cracks under opening mode. J. Eng. Math. **83**(1), 143–168 (2013)
21. Markides, Ch.F., Pazis, D.N., Kourkoulis, S.K.: The centrally cracked Brazilian disc: implications and solutions in case of closing cracks. J. Mech. Beh. Mat. **23**(3–4), 59–77 (2014)
22. Fairhurst, C.: On the validity of the 'Brazilian' test for brittle materials. Int. J. Rock Mech. Min. Sci. **1**, 535–546 (1964)
23. Markides, Ch.F., Kourkoulis, S.K.: Naturally accepted boundary conditions for the Brazilian disc test and the corresponding stress field. Rock Mech. Rock Eng. **46**(5), 959–980 (2013)
24. Lavrov, A., Vervoort, A.: Theoretical treatment of tangential loading effects on the Brazilian test stress distribution. Int. J. Rock Mech. Min. Sci. **39**, 275–283 (2002)
25. Lanaro, F., Sato, T., Stephensson, O.: Microcrack modelling of Brazilian tensile tests with the boundary element method. Int. J. Rock Mech. Min. Sci. **46**, 450–461 (2009)
26. Kourkoulis, S.K., Markides, Ch.F., Hemsley, J.A.: Frictional stresses at the disc-jaw interface during the standardized execution of the Brazilian disc test. Acta Mech. **224**(2), 255–268 (2013)